Article

Not peer-reviewed version

Study and Modeling the Impact of June 2015 Geomagnetic Storms on the Brazilian Ionosphere

Oladayo O. Afolabi * , C.M.N Candido , F. Becker-Guedes , C. Amory-Mazaudier

Posted Date: 3 October 2023

doi: 10.20944/preprints202310.0108.v1

Keywords: Vertical Total Electron Content (VTEC); Prompt Penetration of Magnetospheric Convection Electric Field; Disturbance Dynamo Electric Field (DDEF); DP2; Ddyn

Article

Study and Modeling the Impact of June 2015 Geomagnetic Storms on the Brazilian Ionosphere

Oladayo O. Afolabi [1,2], C.M.N. Candido [2], F. Becker-Guedes [2] and C. Amory-Mazaudier [3]

[1] National Space Research and Development Agency, Abuja, Nigeria; afolabi.olayiwola@inpe.br
[2] Instituto Nacional De Pesquisas Espaciais, Brazil;
[3] Sorbonne Université, Ecole Polytechnique, Institut Polytechnique de Paris, Université Paris Saclay, Observatoire de Paris, CNRS, Laboratoire de Physique des Plasmas (LPP), 75005 Paris, France.
* Correspondence: afolabi.olayiwola@inpe.br.

Abstract: This study investigates the impact of geomagnetic storms that occurred on June 8, 22-23, and 25, 2015, on the ionosphere in the low-latitude and equatorial regions of Brazil. By examining various data sources, such as solar wind parameters from the ACE satellite, GPS vertical total electron content (VTEC), magnetometer data, and the SAMI2 model, we aimed to simulate the effects of storms on the ionosphere in these regions. Two methods were employed to separate DP2 and Disturbance dynamo (Ddyn) from the ionospheric disturbance current (Diono). Our analysis revealed a positive (negative) ionospheric storm in the VTEC during the main phase (recovery) of the June 22-23 and 25 storms. This observation can be attributed to the combined impact of the eastward prompt penetration of the magnetospheric convection electric field (westward disturbance dynamo electric field) and changes in the storm-time thermospheric [O]/[N_2] ratio based on the GUVI satellite imagery. Notably, the westward disturbance dynamo exhibited a significant amplitude on June 23 in Belem. The amplitude of the D_{dyn} at Belem (dip lat: - 0.47°) was greater than that at Alta Floresta (dip lat: - 3.75°) due to intensified cowling conductivity in Belem. Furthermore, we found that the SAMI2 model provided more accurate results when we replaced the default ExB drift with the vertical drift calculated from the ground-based magnetometer, enabling us to simulate the effect of the westward DDEF on VTEC during daytime.

Keywords: Vertical Total Electron Content (VTEC); prompt penetration of magnetospheric convection electric field; Disturbance Dynamo Electric Field (DDEF); *DP2*; D_{dyn}

1. Introduction

The equatorial and low latitude ionosphere (**0°- 30°** North and South of the equator) is often a bubbling fountain of plasma that generates strong electron density gradients. These gradients significantly disturb some types of communication and navigation signals (for example GNSS, High-frequency Radar system) [1]. The equatorial ionosphere presents some phenomena such as Equatorial Ionization Anomaly (EIA), Equatorial Temperature and wind anomaly (ETWA), equatorial trough anomaly (ETA), equatorial plasma bubble, ionospheric scintillations, and Equatorial Spread F (ESF) among others [2–8]. The spatial and temporal fluctuations of the ionized plasma during the day are connected with two crests of ionization: one resides in the southern magnetic hemisphere and the other in the northern magnetic hemisphere and the trough at the magnetic dip equator [9–11]. The diurnal instability of EIA in terms of the latitudinal wideness of crests and relative enhancement, its morphology, climatology, and manifestations during varying geomagnetic conditions, seasons, and solar epochs have been reviewed by many researchers [11], [12]. During the occurrence of the geomagnetic storm, the quiet day morphology of the equatorial ionosphere anomaly can be altered due to the prompt penetration of the magnetospheric electric field (PPMEF) and the disturbance dynamo electric field (DDEF) [5], [11], [13–22]. The geomagnetic disturbance recorded at the ground level is the integration of magnetic disturbances associated with the different current systems flowing in the magnetosphere[16], [17], [23], [24]. Geomagnetic disturbance related to the ionospheric electric currents is mainly due to the intensification of the auroral electrojets at high latitudes [22].

 doi:10.20944/preprints202310.0108.v1

Large-scale ionospheric current systems connecting high and low latitudes are driven by two primary mechanisms. The initial mechanism involves the direct and immediate penetration of the magnetospheric convection electric field (PPMEF) [16], [22]. The second mechanism is attributed to the ionospheric disturbance dynamo electric field (DDEF) [5], [16–18], [22], [23] [25].

This research paper delves into the examination of how the ionosphere in the Brazilian equatorial and low-latitude regions reacted to geomagnetic storms that took place in June 2015. The specific storms examined are those that occurred on 22-23 and 25 June 2015, which were induced by the combination of a coronal mass ejection (CME) and a high-speed solar wind stream (HSSWs) [24–27]. Additionally, the geomagnetic storm occurring on June 8, 2015, was primarily instigated by HSSWs.

Numerous scientists globally have reported the geomagnetic storm that occurred on June 22-23, 2015. Astafyeva conducted a comprehensive study of this storm using multiple instruments, revealing a positive ionospheric storm on the nightside of the summer hemisphere. The researchers attributed this phenomenon to the influence of the eastward disturbance dynamo electric field and storm-time thermospheric circulation, which were further reinforced by the disturbance dynamo electric field (DDEF). Additionally, they documented an intense dynamic variation in the ionosphere during the main phase on the dayside of the northern hemisphere, driven by PPMEF. In contrast, the development of a secondary positive sub-phase of the storm in the southern hemisphere was attributed to factors other than PPEF, indicating an enhanced thermospheric composition during the storm.

In another study on the ionospheric response to the June 22-23, 2015 geomagnetic storm, Mansilla (2018) [26] examined the Global Navigation Satellite System (GNSS) receivers to analyze the Total Electron Content (TEC) and observed TEC depletion at midlatitude stations. But at the equatorial and low latitude stations during the storm's main phase, the enhancements in TEC due to eastward prompt penetration electric field of the under shielding of the R1 region field-aligned current. The winter hemisphere presents short-duration positive ionospheric storms in the dayside and long-duration positive ionospheric storms in the nightside during the main phase in Africa, Australia, and eastern Antarctica [26].

The impact of the 22-23 June 2015 geomagnetic storm was also investigated in some regions by (Astafyeva (2017,2018) at the equatorial and low latitude ionosphere over South America (SA) and Asia sectors by using ground-based instruments (GNSS receivers, ionosondes, magnetometers) and as well as satellites, and reported enhancements in VTEC, electron and ion density on the dayside and a downward vertical drift with a decrease in the VTEC and plasma density in the nightside and they attributed the observed enhancements to the prevailing role of PPMEF[27], [28].

Paul (2018), looked at the latitudinal ionospheric response during the three most prominent geomagnetic storms of 2015 during solar cycle 24 which are 16-17 March 2015, 22-23 June 2015, and 19-22 December 2015 using TEC data derived from a latitudinal chain of Global Positioning System (GPS) receivers that extend from 70°N to 70°S. They observed a symmetrical hemispheric response during the strongest 17th March (St. Patrick's Day) storm whereas the asymmetric hemispheric response of the ionosphere during the 22nd June and 20th December storm over the Asian-Australian sector and the African equatorial and low-latitude sector [29]. Amaechi (2018) examined the effect of the intense geomagnetic storms of 2015 on the occurrence of large-scale ionospheric irregularities over Africa and they concluded that irregularities occurred in the post-sunset to midnight period and were associated with TEC depletions and fluctuations, due to equatorial plasma bubbles, and are stronger over the equatorial ionospheric anomaly (EIA) crest [30].

Singh (2017) investigated the impact of the June 22-23, 2015 geomagnetic storm on the Indian ionosphere using ionosondes. They observed suppressed spread F during the westward penetration electric field of the overshielding R2 region in the Indian sector. Fluctuations in foF2 with shorter periods were attributed to eastward prompt penetration electric field fluctuations, while larger period fluctuations were mainly caused by disturbance wind, TIDs, and DDEFs. Plasma bubbles were suppressed in the Indian sector, in contrast to their detection in the European sector [29].

Macho (2020) studied ionospheric dynamics in the South American sector from June 21-24, 2015. They used ground ionosonde stations, GNSS receivers, Very Low Frequency (VFL), and

Preprints (www.preprints.org) | NOT PEER-REVIEWED | Posted: 3 October 2023 doi:10.20944/preprints202310.0108.v1

magnetometer data. The study revealed an expansion of the crest of the equatorial ionospheric anomaly (EIA) at midlatitudes and high latitudes, mainly due to the prompt penetration electric field during the main phase [30].

In this present study, we concentrate on the effect of the June, 8, 22-23, and 25, 2015 geomagnetic storm on Brazil's equatorial and low-latitude ionosphere. Especially, during the disturbance dynamo electric field event (DDEFe). We used ground-based magnetometer data, GPS TEC data, and the SAMI2 model to quantify the impact of the space weather event on Brazil's longitude.

This research article comprises five distinct sections. The first section commences with an introduction, followed by a comprehensive literature review of prior work. The second section delves into the methodology employed in this study. Moving forward, section three presents our findings, while section four is dedicated to discussing these results in detail. Lastly, in section five, we conclude and summarize the key outcomes of our research.

2. Data Source, Data Processing, and Model

2.1. Data Source

High-resolution Interplanetary parameters in geocentric solar magnetospheric coordinates (GSM) recorded onboard the Advanced Composition Explorer (ACE) satellite were used to monitor solar wind conditions. These were: - the solar wind speed (Vsw), z-component of the interplanetary magnetic field (IMF Bz), y-component of the interplanetary electric field (IEyF), Auroral Electrojet indices (Auroral upper boundary (AU) and Auroral lower boundary (AL)). The data are made available by OMNIWeb data services via http://omniweb.gsfc.nasa.gov/form/omni_min.html. The website was last accessed on August 28, 2023.

Magnetic parameters were also accessed from the high-resolution OMNIWeb data service. These are the Symmetric disturbance in the horizontal direction (SYM-H) and Asymmetric disturbance in the horizontal direction (ASYM-H). All of these data can be accessed on the website of OMNIWeb services data via https://omniweb.gsfc.nasa and last accessed on August 28, 2023.

Equatorial and Low-latitude ionosphere response to magnetic perturbation were examined by using GNSS-TEC obtained by processing GNSS-Rinex files made available by the Brazilian Network for Continuous Monitoring of the GNSS System (RBMC) via http://www.ibge.gov.br. The Map of the geographic coordinates of the GPS stations is shown in Figure 1.

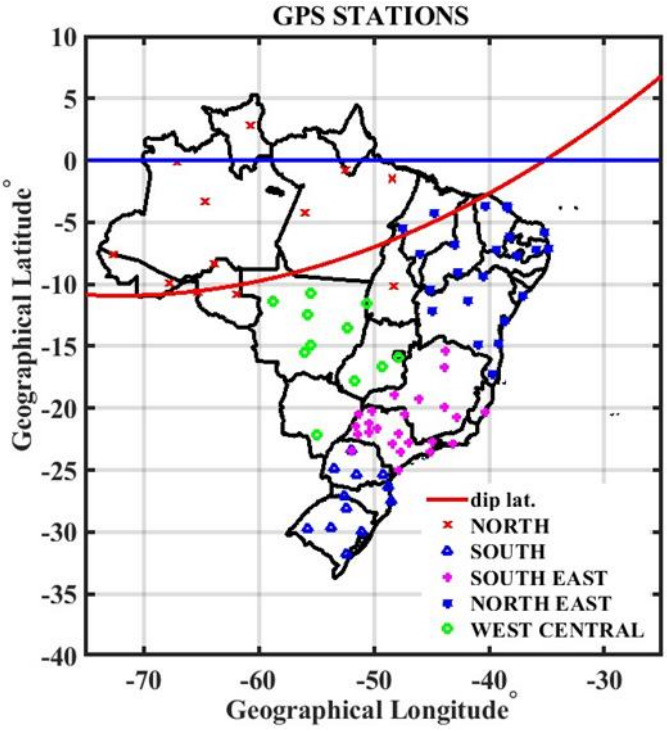

Figure 1. Map of GPS data.

Preprints (www.preprints.org) | NOT PEER-REVIEWED | Posted: 3 October 2023 doi:10.20944/preprints202310.0108.v1

The magnetic data used in this study are obtained from the Study and Monitoring of Brazilian Space Weather (EMBRACE) via http://climaespacial/portal and South American Meridian B-Field Array (SAMBA) through http://magnetometers.bc.edu. Magnetometers are installed in Belem (BELE: -1.41°, -48.18, dip lat. -0.47°), Cuiaba (CUIB: -15.55°, - 56°, dip lat. -8.71°, and Alta Floresta (ALF: -9.87°, -56.10°, dip lat -3.74°) respectively. These magnetometers provide 1 minute of data of the northward (X), eastward (Y), and vertical (Z) components of the Earth's magnetic field. The station's geographic coordinates are shown in Figure 2.

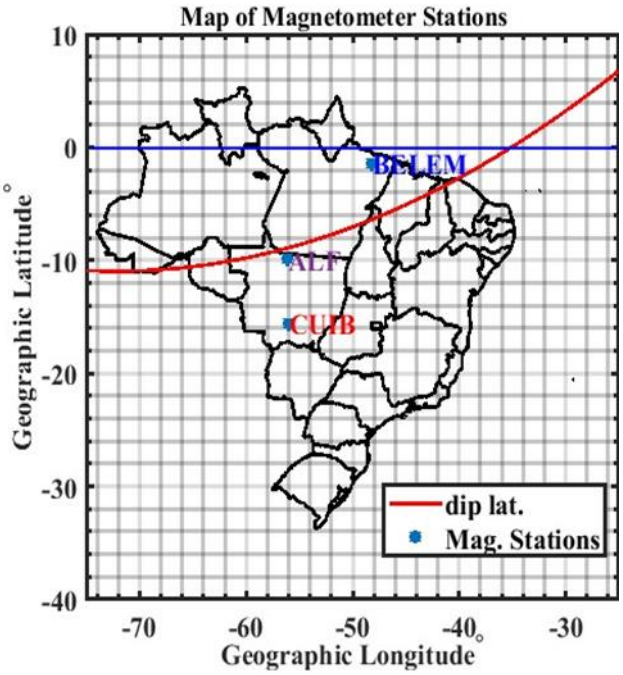

Figure 2. Map of magnetometer data.

2.2. Data Processing

2.2.1. GPS Data

The GPS Receiver Independent Exchange Format (RINEX) files obtained from the Brazilian Network for Continuous Monitoring of GNSS Systems were processed by using the GPS-TEC analysis application software developed by Gopi Seemala and Boston College, United States of America. The details of this GPS-TEC application software can be found in Gopi Seemala (2011) [31].

We compute the TEC-MAP by using one-minute VTEC resolution data. The VTEC data are grid $1^{\circ} \times \mathbf{1}^{\circ}$ in geographical latitude and longitude. The dip latitudes are computed from the website of the British Geological Survey https://geomag.bgs.ac.uk/cgi-bin/coord_calc). The magnetically quiet days are obtained from the International Service of Geomagnetic Indices (ISGI, http://isgi.unistra.fr). We compute the storm-time residual TEC ($\Delta \boldsymbol{TEC}$) by subtracting the five magnetically quiet days *VTEC* from the magnetically disturbed days *VTEC*. Equations (1) and (2) expressed the process of computation of $\Delta \boldsymbol{TEC}$ mathematically.

$$\boldsymbol{Q_{5AVR}} = \frac{\mathbf{1}}{\boldsymbol{N}} \sum_{\mathbf{1}}^{\boldsymbol{N}} \boldsymbol{MQD} \quad (1)$$

Where $\boldsymbol{MQD}$ is the magnetically quiet days. $\boldsymbol{N}$ is the number of the magnetically quiet days. Where $\boldsymbol{Q_{5AVR}}$ is five magnetically quiet days.

$$\Delta \boldsymbol{TEC} = \boldsymbol{MDs} - \boldsymbol{Q_{5AVR}} \quad (2)$$

Where $\boldsymbol{MDs}$ is the magnetically disturbed days.

2.2.2. Computation of Equatorial Electrojet (EEJ)

We compute the horizontal component of the Earth's magnetic field from the X and Y components of the Earth's magnetic field as presented in equation (3).

$$\boldsymbol{H} = \sqrt{\boldsymbol{X^2} + \boldsymbol{Y^2}} \quad (3)$$

Preprints (www.preprints.org) | NOT PEER-REVIEWED | Posted: 3 October 2023 doi:10.20944/preprints202310.0108.v1

To eliminate variations in offset values among different magnetometers, we first calculate the nighttime baseline values for the H component using equation (4) for each day. These baseline values are then subtracted from the corresponding magnetometer data set to obtain the hourly departure of H, which is denoted as $\boldsymbol{\delta H}$ and can be expressed using equation (5). The baseline value is defined as the average of the H-component nighttime (23:00 – 02:00 LT) values of the Earth's magnetic field.

$$\boldsymbol{H_0 = \frac{H_{23}+H_{24}+H_{01}+H_{02}}{4}}, \quad (4)$$

Where $\boldsymbol{H_{23}, H_{24}, H_{01}, and\ H_{02}}$ are respectively the hourly values of $\boldsymbol{H}$ at 23:00, 24:00, 01:00, and 02:00 in local time (LT).

$$\boldsymbol{\delta H = H(t) - H_0} \quad (5)$$

The time variable, t, represents the hours ranging from 01:00 to 24:00 LT. The hourly departure, $\boldsymbol{\delta H}$, is then adjusted for the noncyclic variation using equation (6). This correction method was previously proposed by Rastogi et al. (2004), who defined noncyclic variation as a phenomenon where the value at 01:00 LT differs from that of local midnight (24:00 LT) [32].

$$\boldsymbol{\Delta c = \frac{\delta H_{01} - \delta H_{24}}{23}} \quad (6)$$

The values for the solar quiet variation (Sq) can be obtained by correcting the hourly departure of $\boldsymbol{H(\delta H)}$ for the noncyclic variation based on the magnetometer data set. This relationship is expressed in Equation (7).

$$\boldsymbol{S_q(t) = \delta H(t) + (t-1).\Delta c} \quad (7)$$

Where $\boldsymbol{t = 1}$ to 1440.

By selecting a station inside the EEJ current (Belem dip altitude: - 0.47) and a station outside the EEJ current (Cuiaba dip latitude: -8.71), as shown in equation 8, we determine the Equatorial Electrojet (EEJ).[5], [33], [34].

$$\boldsymbol{\Delta H = H_{BELEM} - H_{CUIABA}} \quad (8)$$

To estimate the vertical drift velocity from the ground-based magnetometer for the daylight plasma drift as given in equation (9) [34, 35], we use multiple regression analysis techniques as suggested by Anderson (2004).

$$\boldsymbol{V_d = 12.26 - 0.0454F10.7 + 0.1892\Delta H + 0.00028\Delta H^2} \text{ - } 0.0000022\boldsymbol{\Delta H^3} \quad (9)$$

Computation of ionospheric disturbance current ($\boldsymbol{D_{dyn}}$).

The ionospheric disturbance electric current $(\boldsymbol{D_{iono}})$ is computed with equation (10). $\boldsymbol{D_{iono}}$ is the magnetic disturbance due to ionospheric electric current system [18], [19], [21], [23], [35], [36]

$$\boldsymbol{Diono = H - H_o - S_R^H - SYMH.\cos\emptyset} \quad (10)$$

Where H is the Earth's horizontal magnetic field's measured component, ∅ is the magnetic latitude of the stations, and, $\boldsymbol{S_R^H}$ is the daily regular fluctuation of H caused by the solar quiet $(\boldsymbol{S_q})$ system, $\boldsymbol{S_R^H}$ is calculated by averaging five magnetic quiet days provided by the World Data Centre Kyoto for Geomagnetism (Kyoto-u.ac.jp). $\boldsymbol{D_{iono}}$ is the total of the magnetic disturbance related to the disturbance polar number 2 (DP2) fluctuations during the prompt penetration of the magnetospheric convection electric field (PPMEF) and the magnetic disturbance dynamo electric field (DDEF) associated with the disturbance dynamo $\boldsymbol{(D_{dyn})}$, as shown in equation (11) [19], [36–39].

$$\boldsymbol{Diono = DP2 + D_{dyn}} \quad (11)$$

Ionospheric electric current disturbance $(\boldsymbol{D_{iono}})$ is the sum of DP2 and Ddyn. We focused on the $\boldsymbol{D_{dyn}}$'s impact on Brazilian equatorial stations during the recovery phase in this article. We utilized two techniques to isolate the effect of DP2 and $\boldsymbol{D_{dyn}}$ on the Brazilian equatorial ionosphere:

i. The diurnal component of the disturbance dynamo is identified by multiresolution analysis (MRA) of the maximum overlap discrete wavelet transform (MODWT) on $\boldsymbol{D_{iono}}$. And for DP2 fluctuation, we select the wavelet component with a period of four hours at maximum [40–42].

ii. Semblance cross-correlation wavelet analysis [35], [43]. We refer interested readers to check the article published by Younas (2021) [35], [43], [44]. We perform semblance analysis by comparing the local phase relation between Sq current and $\boldsymbol{D_{iono}}$ current as a function of time and wavelength. The detail of this new method to identify the anti-Sq from the Diono can be found in the [35]. The positive phase is represented by +1 and the negative phase is represented by -1 (which anti-Sq current).

Preprints (www.preprints.org) | NOT PEER-REVIEWED | Posted: 3 October 2023 doi:10.20944/preprints202310.0108.v1

2.2.3. Computation of Akasofu's parameter

When the interaction between the solar wind and magnetosphere is intensified, it results in the generation of powerful magnetospheric currents and an increase in the magnetic energy density within the magnetosphere. This energy leads to the restructuring of the magnetosphere, faster movement of plasma in the plasmasheet, heating and acceleration of particles, as well as the amplification of currents [45], [46]. The movement of solar wind particles about the Earth generates a flux of kinetic energy. This energy flux in the plasma plays a crucial role in shaping the magnetosphere. Additionally, the interplanetary magnetic field influences the magnetosphere through a flux known as the Poynting flux [1], [46].

Poynting flux is the power delivered by electromagnetic sources. Akasofu (1981) produced an electromagnetic power flux estimate that represents the solar wind power delivered by the magnetic merging equation (12). He assumed that only the tangential component, $\boldsymbol{B_t}$ of the IMF delivers energy, so the $\boldsymbol{B_x}$ component does not play a role. The elements in the square bracket of equation (12) constitute the poynting flux. The factor outside the bracket accounts for the efficiency of energy entry by an anti-parallel component of the IMF.

$$\boldsymbol{P = \left[\left(1/\mu_0\right)(E_{SW} \times B_{SW})\right]\left(\sin\left(\theta/2\right)\right)^4 = \left(1/\mu_0\right)v_{SW}|B_t|^2\left(sin\left(\theta/2\right)\right)^4} \qquad (12)$$

Where:

$\boldsymbol{P}$ = **effective solar wind poynting flux** $[\boldsymbol{W/m^2}]$

$\boldsymbol{\mu_0}$ = **permeability of free space** $(\boldsymbol{1.26 \times 10^{-6}\ N/A^2})$

$\boldsymbol{v_{SW}}$ = **solar wind velocity** $[\boldsymbol{m/s}]$

$|\boldsymbol{B_t}|$ = magnitude of the tangential component of the IMF = $\sqrt{\boldsymbol{B_y^2 + B_Z^2}}$ $[\boldsymbol{T}]$

$\boldsymbol{\theta}$ = IMF polar angle in the Y-Z GSE plane $\left(\boldsymbol{tan^{-1}\left(B_y/B_z\right)}\right)$ $[\textbf{deg } \boldsymbol{or\ rad}]$

For many storm-time applications, space weather scientists are most interested in the power delivered to the cross-section of the dayside magnetosphere. One version of the power estimate, called the Akasofu epsilon parameter $(\boldsymbol{\varepsilon})$, comes from multiplying the effective solar wind poynting flux by a factor proportional to cross-sectional area of the magnetopause that intercepts the solar wind as shown in equation (13):

$$\boldsymbol{\varepsilon = \left(1/\mu_0\right)v_{SW}|B_t|^2\left(sin\left(\theta/2\right)\right)^4 l^2} \qquad (13)$$

Where:

$\boldsymbol{\varepsilon}$ = Akasofu epsilon parameter $(\boldsymbol{W})$

$\boldsymbol{l^2}$ = effective cross-sectional area of the merging region $\approx (\boldsymbol{7R_E})^2$

Scientists frequently utilize ε as a reference point when analyzing the energy distribution in magnetic storms. Nevertheless, in the case of severe storms, this estimation may become inaccurate due to significant fluctuations in the cross-sectional area of the magnetopause or the influence of other factors that are not well comprehended, which can impact the efficiency of energy transfer [1], [45], [46].

2.3. SAMI2 Model

SAMI 2 (Another Model for ionosphere) calculates the evolution of the ionosphere in the low- to mid-latitudes. SAMI2 considers the dynamic plasma and chemical changes of seven ion species $(\boldsymbol{H^+, He^+, N^+, O^+, N_2^+, NO^+, and\ O_2^+})$ within the altitude range of 85 km to 20, 000 km. This altitude range corresponds to a latitudinal span of approximately $\boldsymbol{\pm 62.5^\circ}$ around the magnetic equator [47].

SAMI2 solves the ion continuity and momentum equations for all seven ion species. Additionally, it solves the temperature equation for $\boldsymbol{H^+, He^+, O^+}$ and the electrons. The code models the plasma along the Earth's geomagnetic field, spanning from one hemisphere to the other. It utilizes an offset, tilted dipole field for this purpose.

The code incorporates a modeled E x B drift of the plasma, which represents the motion of the plasma due to the interaction between the electric field (E) and the magnetic field (B). It also considers ion inertia in the ion momentum equation to account for motion along the dipole field line.

 doi:10.20944/preprints202310.0108.v1

SAMI2 employs a fixed, nonorthogonal grid, where one coordinate axis aligns with the geomagnetic field. The neutral species are characterized using the empirical models NRLMSISE00 and HWM14. These models provide information about the neutral atmosphere, which is essential for understanding the behavior of the ionosphere [47], [48].

The input parameters into SAMI2 model are value of F10.7A (3 months average of F10.7), daily value of F10.7, daily value of Ap, year, day. SAMI2 code is coupled with NRLMSISE00, HWM14, EUVAC model developed by Phil Richchards [49]. By default, it assumes that the ionosphere's perpendicular vertical E × B drift, which is influenced by the magnetic field, can either be sinusoidal or defined by the E × B drift model [50].

The primary output of SAMI2 model include: - ion density, ion temperature, ion velocity along magnetic field, electron temperature, time step in local time, geographic latitude, geographic longitude, altitude. The detail about SAMI2 model can be found in article published by Hubal et al (2000) [47].

3. Results

3.1. Impact of June 22-23, and 25 Geomagnetic Storm Brazilian Ionosphere

3.1.1. The state of the interplanetary medium from 20-30 June 2015

The fluctuations in the solar wind parameters from June 20-30, 2015, are shown in Figure 3. A magnetic quiet reference day has been selected for June 20, 2015. The initial interplanetary shock (IS) caused the SYM-H index to rise to ~ 40 nT (Figure 3e) on June 21 at 16:45 UT (13:45 LT) and it did not trigger in any aurora activity at high latitude, as can be seen in Figure 3d. The second IS hit the earth's magnetic field on June 22, 2015, at approximately 05:45 UT (02:45 LT) and it triggers a considerable increase in aurora electrojet activity, the solar wind velocity increased from 350 to 400 km/s, the IMF Bz and interplanetary east-west electric field (IEyF) oscillates rapidly, and the SYM-H index also increase from 0 to 20 nT. On June 22, 2015, at 18:38 UT (15:38 LT), the third and largest IS made contact with the earth's magnetic field. The IMF Bz turned southward and achieved a minimum of - 40 nT, while the IEyF turned eastward and reached a maximum positive value of 27 mV/m. The solar wind velocity increased from 400 to 720 km/s. This signaled the abrupt start of the geomagnetic storm's main phase, which occurred between June 22 and 23, 2015. The plot of the equatorial Electrojet is shown in Figure 3f. The eastward prompt penetration of the magnetospheric electric field (EPPMEF) during the main phase from 18:38 to 20:00 UT (15:38 - 17:00 LT) caused the increase in EEJ on June 22 [18], [20], [24], [25], [27], [40], [45]. The interested reader can obtain a thorough account of the interplanetary medium's condition during this storm in Astafyeva et al, 2017, 2018, [25], [46]. Around 20:00 UT (17:00 LT), the IMF Bz turned northward and continued to oscillate northward and southward until around 01:30 UT on June 23, 2015. From 2:00 UT till 06:00 UT, it later turned south. At 04:45 UT, the SYM-H index reached its minimum southward incursion of -208 nT (01:45 LT).

The storm recovery began gradually at 04:45 UT, coinciding with the Earth's magnetic field being impacted by the high-speed solar wind stream (HSSWs). Figure 3f shows that on June 23, 2015, the westward disturbance dynamo electric field (WDDEF) influenced the westward flow of the Equatorial Electrojet (EEJ) from 13:00 UT (10:00 LT) until 23:00 UT (20:00 LT).

On June 24, the magnetic field of the Earth encountered yet another Interplanetary Shock (IS). As evident from observations, at 13:00 UT, the speed of the solar wind was approximately 700 km/s, although it did not have a significant impact on Earth's magnetic field. However, on June 25, a fresh IS emerged, leading to a moderate geomagnetic storm. By approximately 19:30 UT (16:00 LT), the SYM-H index reached a negative value of -89 nT.

From June 25 to June 29, 2015, the Equatorial Electrojet (EEJ) exhibits a decreased magnitude in comparison to the average value observed during five days of magnetic quietness. Remarkably, on June 30th, the amplitude of the EEJ closely matched that of a typical magnetic quiet day, indicating a full recovery of the Brazilian low latitude ionosphere to its quiet state.

Preprints (www.preprints.org) | NOT PEER-REVIEWED | Posted: 3 October 2023 doi:10.20944/preprints202310.0108.v1

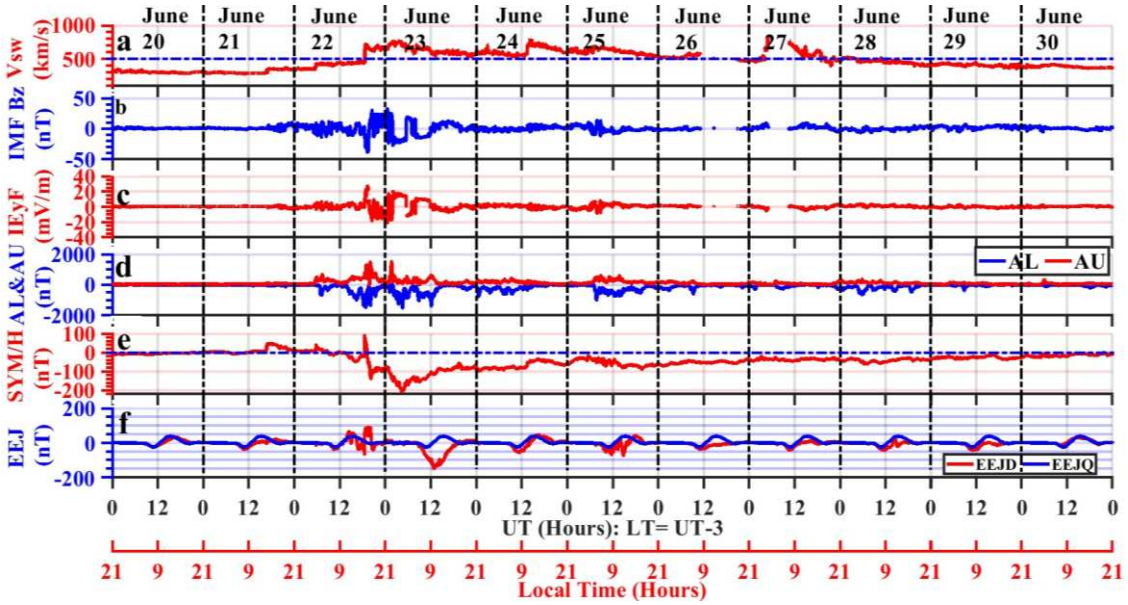

Figure 3. The state of the interplanetary medium from June 20 to 30, 2015. (a) displays the velocity of the solar wind. Figure 3b exhibits the IMF Bz (Interplanetary magnetic field in the Z direction), (c) presents the interplanetary electric field, (d) portrays the aurora electrojet (AL: aurora lower boundary, AU: aurora upper boundary), (e) demonstrates the H-component symmetry of Earth's magnetic field observed at various low-latitudes, and lastly, (f) illustrates the equatorial electrojet (EEJ) at Belem (dip lat: - 0.47).

3.1.2. Brazilian Equatorial Latitude Response to The Magnetospheric Convection

Electric Field.

In Figure 4, we present the variation of IMF Bz, dBz/dt, and DP2 along the Brazilian longitude (specifically, Belem: -0.47°, and Alta Floresta: -3.75° dip latitude). To analyze this data, we utilized the first method described in subsection 2.2.3i.

From June 20-21, 2015, geomagnetic activities are at minimum. But on June22, when the IMF Bz (Figure 4a) turned southward around 18:38 UT, a remarkable observation was made. *DP2* began to fluctuate and reached the maximum amplitude of $\pm \mathbf{25}\ \boldsymbol{nT}$ between 19:00 UT and 20:00 UT on June 22 (Figure 4c). Amplitude of *DP2* at Belem (red legend) almost matched the amplitude of *DP2* at Alta Floresta (blue legend) during the main phase on June 22. The enhancement in *DP2* fluctuation can be attributed to the response to the dawn to dusk magnetospheric electric field convection that penetrate into the Brazilian equatorial ionosphere on June 22, 2015 during the southward incursion of the IMF Bz [38], [39].

Moreover, despite IMF Bz being southward during the night on June 23 as seen in Figure 4c. The amplitude of DP2 fluctuation is very small at Belem and Alta Floresta. This is because the conductivities of the E- region during these periods is very weak [45], [51].

Preprints (www.preprints.org) | NOT PEER-REVIEWED | Posted: 3 October 2023 doi:10.20944/preprints202310.0108.v1

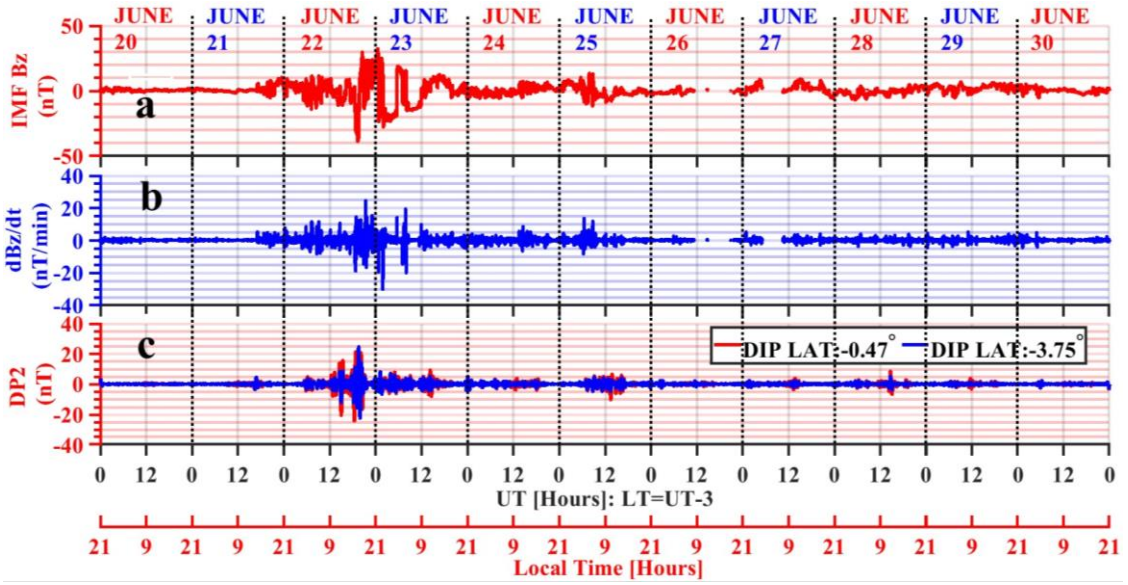

Figure 4. Variation of IMF Bz along with dBz and DP2, (a) displays IMF Bz, (b) shows dBz/dt, (c) illustrates DP2 over Belem (red) and Alta Floresta (Blue).

3.1.3. Development of D_{dyn} during June 22-23, and 25, 2015 Geomagnetic Storm at **Brazilian Longitude.**

Figure 5 illustrates the diurnal variation of the disturbance dynamo (D_{dyn}) at two magnetometers locations, Belem and Alta Floresta. Figure 5a, presents plots of the AE index (red legend) and the Akasofu parameter (blue legend). Figure 5b displays the ASYM-H index, while Figure 5c shows the diurnal component of D_{dyn} at Belem and Alta Floresta.

At Belem, the strength of D_{dyn} is notably greater than the strength of D_{dyn} at Alta Floresta. This disparity is as a result of the enhanced cowling conductivity at Belem [22]. On June 22, in Belem during the main phase, the westward strength of D_{dyn} at 20:00 UT (17:00 LT) is -15.52 nT and at Alter Floresta is -20 nT at 22:00 UT (18:00 UT). The maximum amplitude of the ASYM-H is 363 nT at 20:00 UT on June 22 and the maximum magnitude of the AE index at this time is 2800 nT which also matched the maximum amplitude of the Akasofu parameter which is $2.5 \times \mathbf{10^8}$ *GW*. On June 23, the maximum eastward strength of D_{dyn} is 38 nT at 05:00 UT (02:00 LT) and the minimum westward strength is -51.20 nT at 15: 00 UT (12:00 LT) in Belem. In Alta Floresta on June 23, maximum eastward strength was 20.67 nT at 07:00 UT (04:00 LT) and the minimum westward strength was -15.63 nT at 17:00 UT (14:00 LT).

On June 23, 2015, on the dayside, we recorded the maximum westward strength of disturbance dynamo from 09:00 to 20:00 UT during the recovery phase of the June 22-23, 2015 geomagnetic storm. This phenomenon can be attributed to the time that the recovery phase began and the significant joule heating at high latitudes, as indicated by the AE index in Figure 5a [52]. The recovery phase commenced at 01:45 LT, providing ample time for the disturbance wind to develop and corotate with the Earth to the dayside. As a result, it became geoeffective, leading to the development of a westward D_{dyn}. This westward D_{dyn}, in turn, caused a westward flow of the Equatorial Electrojet (EEJ), as observed in Figure 5c [54].

Figure 5b displays the ASYM-H index shows significant energy input into the low latitude ionosphere on June 22 and June 23, 2015. Additionally, the Akasofu parameter indicates a substantial deposition of energy into the magnetosphere due to the coupling between the solar wind and the magnetosphere on the dayside during the main phase of the geomagnetic storm on June 22, 2015 [1], [54].

Preprints (www.preprints.org) | NOT PEER-REVIEWED | Posted: 3 October 2023 doi:10.20944/preprints202310.0108.v1

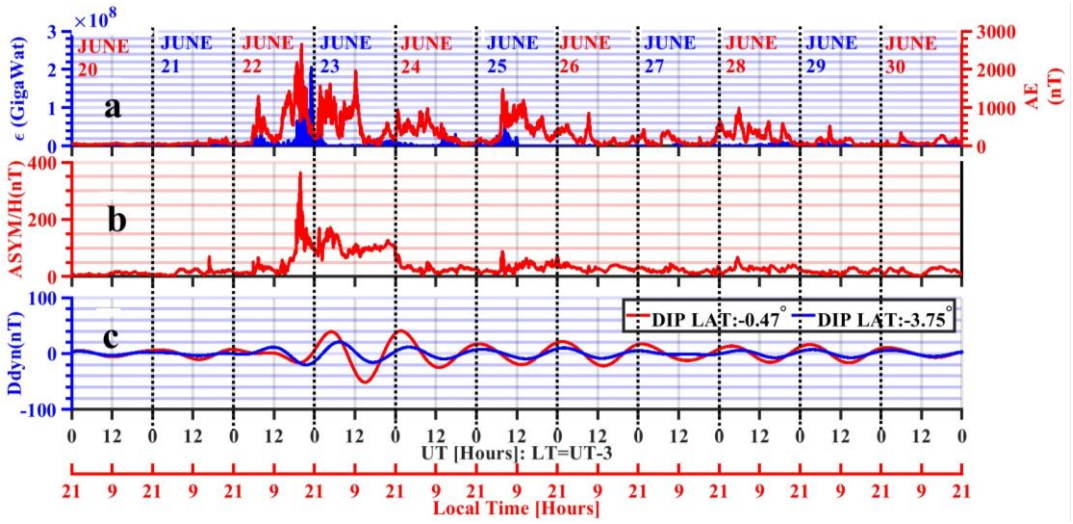

Figure 5. illustrates the evolution of Ddyn at the Brazilian Longitude. (a) The left-hand side displays the AE index, while the right-hand side shows the Akasofu index. (b) Depicts the AYSM-H index, which represents the response to auroral substorms at high latitudes. Lastly, (c) presents the development of $\mathbf{D_{dyn}}$ at Belem (indicated by the red legend) and Alta Floresta (indicated by the blue legend).

3.1.4. Phase Comparison between S_q and Diono Current at Belem Magnetic Station.

Figure 6 shows the phase correlation and anti-correlation between the S_q and Diono current. Figure 6a is the five-day average of magnetically quiet days and Figure 6c is the ionospheric disturbance current ($\boldsymbol{D_{iono}}$). The details of this method can be found in the work of Younas et al, 2022, Terrence and Campo et al, 1998, and Cooper and Cowan, 2008 [35], [43], [44]. Figures 6b and 6d represent the continuous wavelet transform of the S_q and $\boldsymbol{D_{iono}}$ current respectively. Figure 6e shows the semblance between the S_q and $\boldsymbol{D_{iono}}$ current. where + 1 means perfect semblance (red) and -1 no semblance which corresponds to the anti-S_q and is related to the D_{dyn} [23], [43], [44]. Figure 6e shows the amplitude of the $\boldsymbol{D_{iono}}$. We observed strong development of the anti-S_q on June 23, 2015, which represents the development of $\boldsymbol{D_{dyn}}$. Although D_{dyn} has started to develop since the late hours of June 22, 2015, which shows a competition between the eastward prompt penetration electric field and the disturbance dynamo electric field during the main phase.

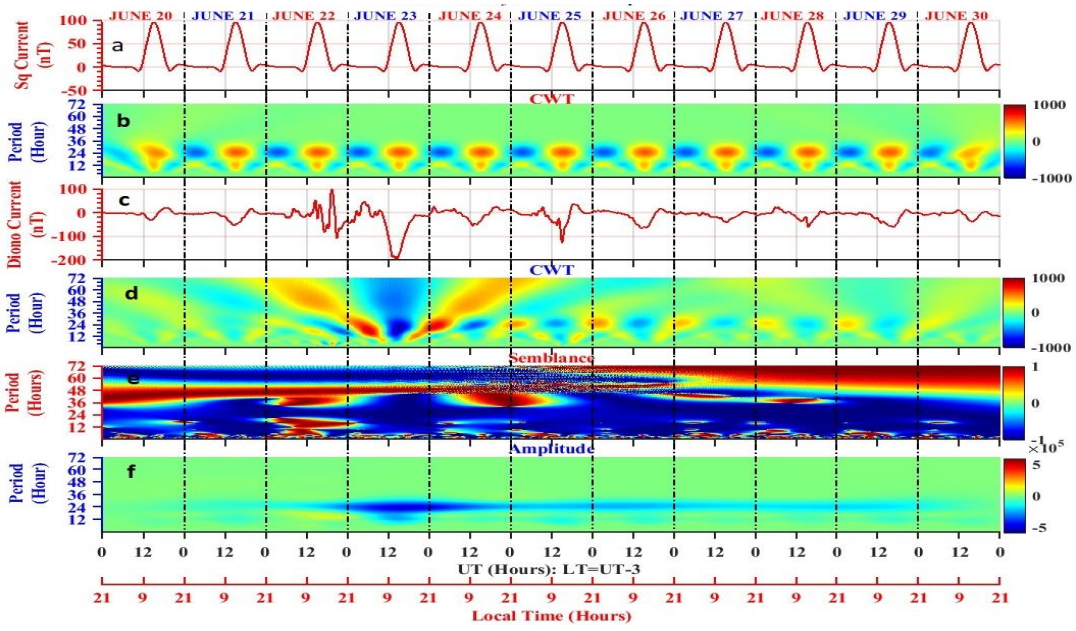

Figure 6. illustrates the relationship between Sq current and Diono current, showcasing both phase correlation and anti-correlation. (a), The average Sq current is displayed for five geomagnetically quiet days in June 2015.

Preprints (www.preprints.org) | NOT PEER-REVIEWED | Posted: 3 October 2023 doi:10.20944/preprints202310.0108.v1

(b) exhibits the continuous wavelet transform of the Sq current depicted in (a). (c) represents the Diono current observed from June 20 to 30, 2015. The continuous wavelet transform of the Diono current in Figure 6c is shown in (d). (e) presents a map indicating the anti-correlation (-1) and correlation semblance (+1) between Diono and Sq current. Lastly, (f) displays the amplitude of the semblance analysis.

3.1.5. Effect of Cowling Conductivity on Strength of D_{dyn}.

The equatorial electrojet is the eastward current that flows along the dip equator by day and produces a large variation of the magnetic field [33], [53]. Close to the magnetic equator, the magnetic inclination angle $(\boldsymbol{I})$ is approximately zero $(\boldsymbol{I} \approx \boldsymbol{0})$. At the E-region, the winds sweep the ions and leave the electrons behind. Electrons are not affected because the collision frequency with the neutral particle is much smaller than the gyro-frequency.

Due to the hall effect, we have:

$$\boldsymbol{J_H = \sigma_H E_x} \quad (14)$$

This current cannot flow through the layer and the charges are accumulated on its borders. The accumulated charges give rise to an upward electric field $(\boldsymbol{E_z})$. The vertical current can not flow as the situation is considered in a steady state. Then there arises a current to cancel the Hall current which is called the Pedersen current equation (15).

$$\boldsymbol{(J_p = \sigma_p E_z)} \quad (15)$$

This implies that

$$\boldsymbol{\sigma_H E_x = \sigma_p E_z} \quad (16)$$

$$\boldsymbol{E_z = \sigma_H E_x / \sigma_p} \quad (17)$$

The zonal current is calculated by adding up the current produced by $(\boldsymbol{E_z \times B})$ that is Hall current with the current due to $\boldsymbol{E_X}$ (Pedersen current).

$$\boldsymbol{J_x = \left(\frac{\sigma_H^2}{\sigma_P^2} + 1\right)\sigma_p E_x = \sigma_c E_x} \quad (18)$$

$$\boldsymbol{\sigma_c = \left(1 + \frac{\sigma_H^2}{\sigma_P^2}\right)} \quad (19)$$

Equation (19) is the cowling conductivity which is responsible for the intensification of the electrojet at the magnetic Equator.

Figure 7 displays the development of D_{dyn} at the Belem (dip lat: -0.47˚) and the at Alta Floresta (dip alt: -3.75˚). The high intensity of the D_{dyn} at the Belen station is attributed to the stronger cowling conductivity at the Belem than at the Alta Floresta [23], [53], [54].

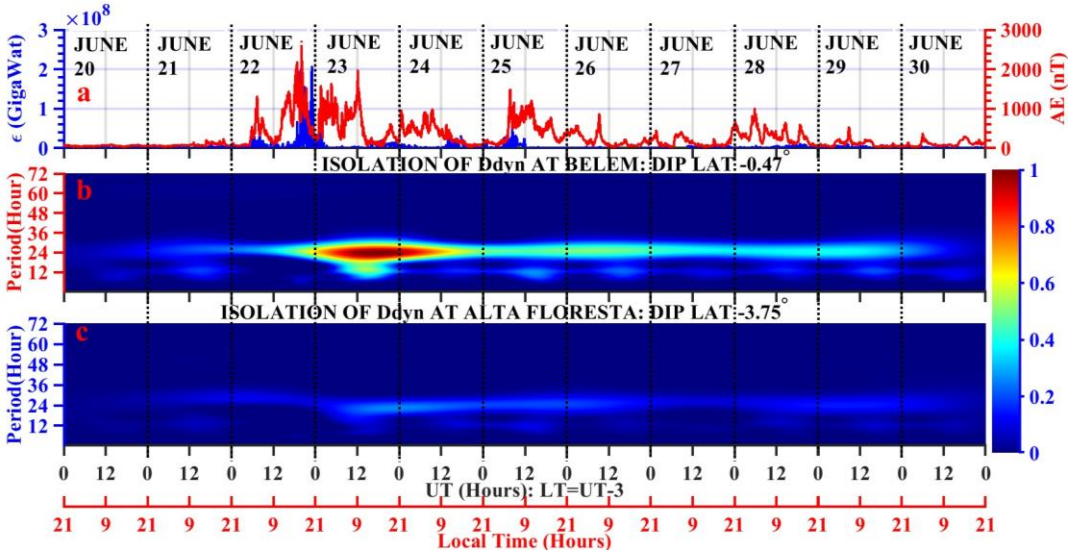

Figure 7. showcases the intensification of $\boldsymbol{D_{dyn}}$ at Belem during a geomagnetic storm. (a) The AE index is displayed on the right-hand side, while the Akasofu parameter is shown on the left-hand side. (b) presents the amplitude of $\boldsymbol{D_{dyn}}$ specifically at Belem. Lastly, (c) illustrates the amplitude of $\boldsymbol{D_{dyn}}$ at Alta Floresta.

Preprints (www.preprints.org) | NOT PEER-REVIEWED | Posted: 3 October 2023 doi:10.20944/preprints202310.0108.v1

3.1.6. Manifestation of The Magnetic Perturbation on The Vertical Total Electron.

Figure 8 depicts the temporal variation of the SYM-H index (Figure 8a), the vertical drift velocity (VDV, Figure 8b), and the VTEC from Figure 8c to Figure 8l from June 20-30, 2015. June 20, SYM/H index is at zero value meaning that the magnetic activities are in a quiet state. But at the commencement of the geomagnetic storm on June 22, 2015, the vertical drift velocity shows a notable increase from 18:38 UT until 20:00 UT. We record an enhancement in the disturbance vertical total electron content from 18:38 until 20:00 UT on June 22 at all the Brazilian GPS stations. The enhancement in VTEC is a combine effect of the eastward prompt penetration of the magnetospheric convection electric field which lifts the ionosphere to a height of reduced recombination rate [13], [55], [56] where the ration of the thermospheric $[\boldsymbol{O}]/[\boldsymbol{N_2}]$ composition is great. The enhancement in VTEC at nighttime on June 23 is attributed to the eastward disturbance dynamo electric field which marks the arrival of the disturbance wind that is richer in the atomic oxygen than in the molecular species. During the daytime, on June 23, from 10:00 UT until 20:00 UT, the vertical drift velocity (Figure 8b) is downward. This implies that the ionosphere has been lowered to the altitude where the ration of thermospheric $[\boldsymbol{O}]/[\boldsymbol{N_2}]$ is low and recombination rate is very high which imply that the equatorward disturbance wind is richer in molecular species than the atomic oxygen and thereby driving negative ionospheric storm from 9° to -12° dip latitude but less significant from -19° to -23° dip latitude [52], [57], [58].

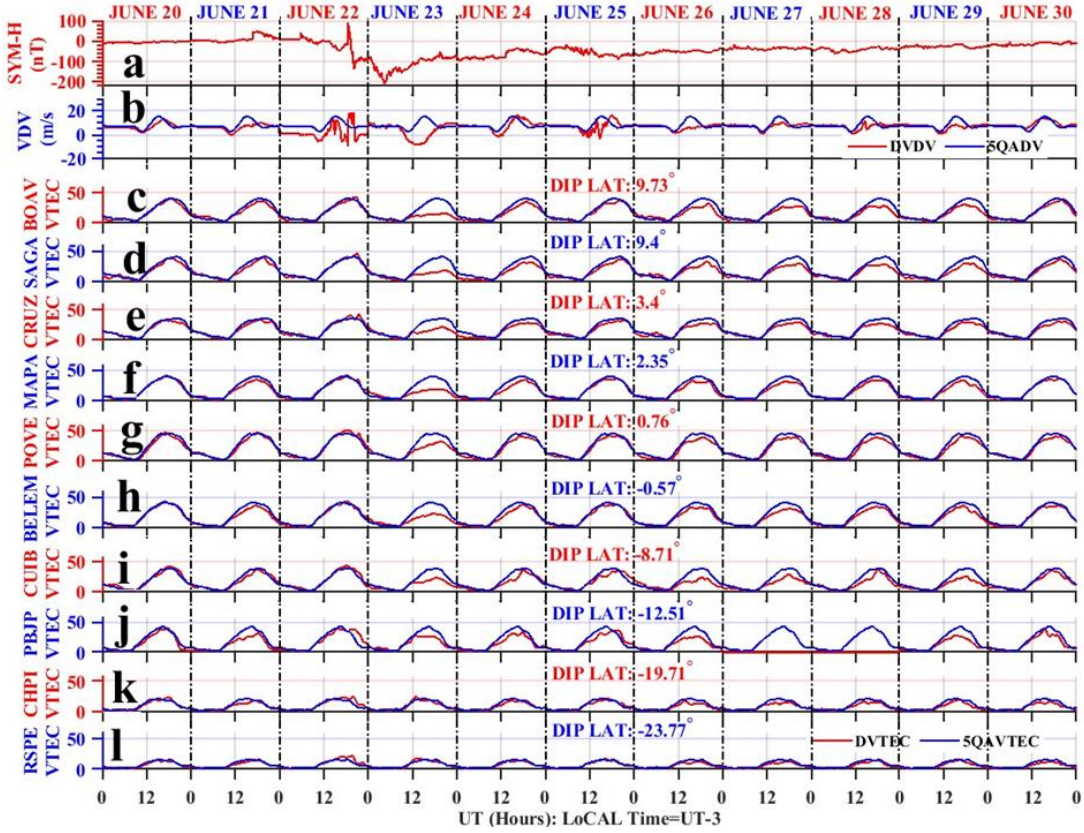

Figure 8. Temporal Variation of VTEC during the occurrence of June 22-23, 25 Storm. (a) shows the day-to-day variation of the SYM-H index. (b) presents the vertical drift velocity that we estimated from ground-based magnetometer from June 20 to 30, 2015 (blue legend (five magnetically quiet days average), red legend (vertical drift velocity from June 20 to 30)). (c) to (l) present the temporal variation of VTEC at different latitudes from June 20 to 30, 2015.

3.1.7. Spatial-Temporal Variation of Vertical Total Electron Content From 20-30 June.

In Figure 9, we analyze how the geomagnetic disturbance affects the Equatorial Electrojet (EEJ), the $\boldsymbol{D_{iono}}$ current, and the spatial-temporal changes in Vertical Total Electron Content (VTEC). Figure 9a displays the influence of the $\boldsymbol{D_{iono}}$ current (red legend) on the storm time residual of EEJ

Preprints (www.preprints.org) | NOT PEER-REVIEWED | Posted: 3 October 2023 doi:10.20944/preprints202310.0108.v1

(ΔEEJ). Figure 9b presents the day-to-day variation of VTEC from June 20 to June 30, 2015. On the right-hand side of the Figure 9b, is the plot showing the SYM-H index, which correlates the intensity of the ring current with the reduction of the earth's horizontal magnetic field during the geomagnetic storm [44], [45]. Figure 9c presents the disturbance VTEC which was calculated by the processes enumerated in section 2.2.1

On June 20, a magnetically quiet reference day, no significant disturbances were observed. However, on June 22, a sudden storm commencement led to an enhancement in both the Equatorial Electrojet (EEJ) and the $\boldsymbol{D_{iono}}$ currents from 18:38 UT to 20:00 UT. The EEJ reached peak value of 88 nT around 20:00 UT (17:00 LT), while the $\boldsymbol{D_{iono}}$ current shows an enhancement of approximately 100 nT at the same time. Figure 9a shows the effect of the Dynamo current on the Storm-time residual ΔEEJ [44].

On June 21, from 12:00 UT until 15:00 UT, close to the arrival time of the first Interplanetary shock, a negative ionospheric storm was observed between dip latitudes ~ -8˚ to -20˚. During June 22's main phase on the dayside, a notable enhancement in VTEC was observed in the southern hemisphere, ranging from ~ -5˚ to -24˚ dip latitude. This positive ionospheric storm correlates with the minimum value of the SYM-H index on the dayside and ranged between 10 TECu and 20 TECu from 18:38 UT to 23:00 UT at the Brazilian low-latitude ionosphere.

On the nightside of June 23 during the main phase (from 23:00 UT until 04:45 UT - 20:00 to 01:45 LT), a moderate enhancement in VTEC was observed from dip latitude 10˚ to -15˚. This enhancement can be attributed to the eastward disturbance dynamo electric field and the injection of energetic particles from the magnetosphere, causing weak ionization along with the storm time equatorward wind, rich in oxygen atom content [13], [14], [41], [42].

During the recovery phase on June 23 (from 09:00 UT to 20:00 UT), 2015, a negative ionospheric storm occurred during the daytime. This negative ionospheric storm is associated with the westward disturbance dynamo, which lowered the ionosphere downward to a region of high recombination rate, coupled with composition changes due to the decrease in thermospheric composition ratio of $[\boldsymbol{O}]/[\boldsymbol{N_2}]$ [25], [26], [41], [42], [45].

On June 24, another Interplanetary shock hit the Earth's magnetic field, causing a moderate geomagnetic storm on June 25, 2015, at 06:00 UT. This results in a positive ionospheric storm in the southern hemisphere between dip latitudes of -2˚ to -20˚. VTEC increased between 10 TECU and 15 TECU starting from 20:00 UT on June 25 to 02:00 UT on June 26. From June 26 to June 30, 2015, varying intensities of negative ionospheric storms (ranging from -10 TECu to -20 TECu) were observed during the daytime (from 12:00 UT to 21:00 UT).

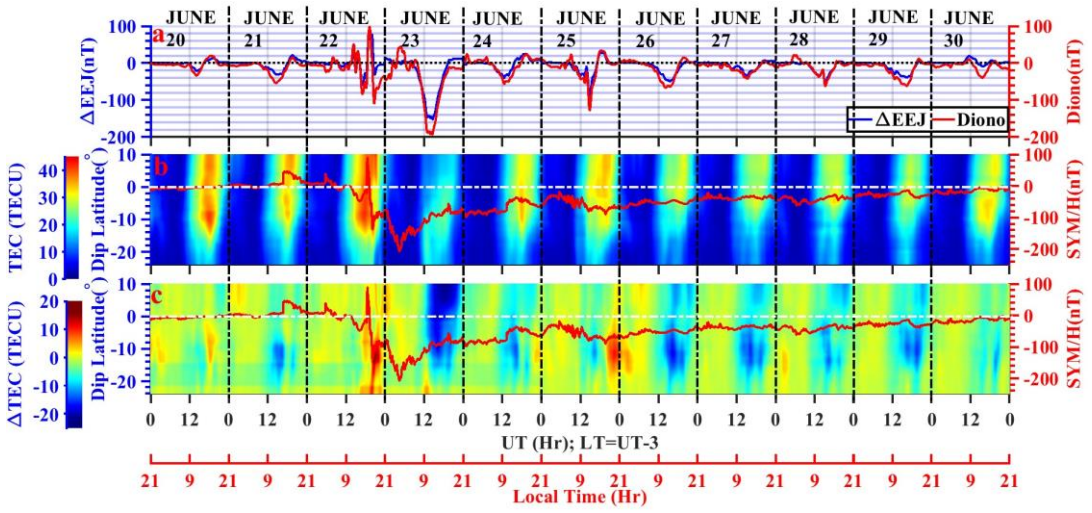

Figure 9. illustrates the spatial-temporal variation of *VTEC* alongside with Δ*EEJ* and $\boldsymbol{D_{iono}}$. (a) Change in *EEJ* and $\boldsymbol{D_{iono}}$ current from June 20 to June 30, 2015. (b) Day-to-day variation of *VTEC* (left-hand side) and *SYM-H*

Preprints (www.preprints.org) | NOT PEER-REVIEWED | Posted: 3 October 2023 doi:10.20944/preprints202310.0108.v1

index (right-hand side). (c) Change in *VTEC* from June 20 to June 30, 2015, (left-hand side) and SYM-H index on right-hand side.

3.1.8. Thermospheric Condition

Figure 10 is the GUVI satellite imagery of the thermosphere from June 20 -25, 2015. June 20 depicts a quiet reference day. On June 22, we noticed an enhancement in thermospheric composition of $[\boldsymbol{O}]/[\boldsymbol{N_2}]$ ratio in a region where there is data availability in the South American region, especially in the northern hemisphere and some part of the southern hemisphere of South America. The enhancement in thermospheric composition of $[\boldsymbol{O}]/[\boldsymbol{N_2}]$ ratio is consistent with enhancement in TEC on June 22 during the daytime as we have seen in Figures 8 and 9. On June 23, 2015, the reduction in the thermospheric composition of $[\boldsymbol{O}]/[\boldsymbol{N_2}]$ ratio in the South American region is consistent with the occurrence of negative ionospheric storm on June 23 according to Figures 8 and 9. On June 24, the intensity of the negative ionospheric storm was reduced compared to the intensity on June 23. This observation is consistent with the reduction in the strength of the westward disturbance dynamo on June 24, 2015, as seen in Figure 5 to 7. Here, we see that the dawn to dusk electric field due to the undershielding of the R1 field align current (R1 FAC) enhances the eastward ionospheric electric field on the dayside [59], [60], and in turned enhances the upward EXB drift velocity which lift the low-latitude ionosphere to the altitude of low recombination rate where ratio of atomic oxygen concentrations is greater than the nitrogen molecule concentration. This mechanism favours the occurrence of positive ionospheric storm. The development of the disturbance dynamo especially, westward component during the daytime lowers the ionosphere to the lower altitude where the nitrogen molecule concentration is higher than the atomic oxygen concentration. This mechanism favours the occurrence of the negative ionospheric storm on the dayside in the low-latitude ionosphere.

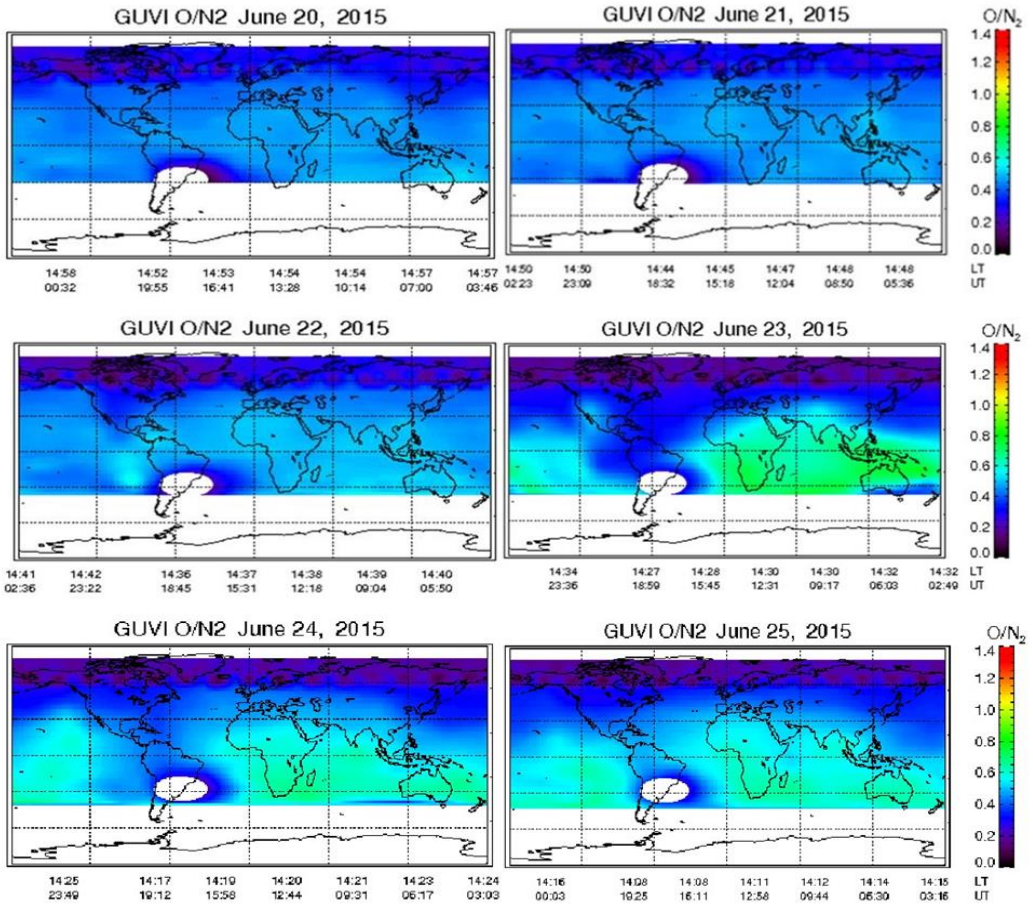

Figure 10. A sequence of six dayside maps of [O/N2].

3.2. Impact of June 8 Geomagnetic Storm on Brazilian Low-Latitude Ionosphere

Preprints (www.preprints.org) | NOT PEER-REVIEWED | Posted: 3 October 2023 doi:10.20944/preprints202310.0108.v1

3.2.1. The state of the Interplanetary Medium from June 6-30, 2015

Figure 11 represents the state of the interplanetary medium from June 6 to June 30, 2015. The high-speed solar wind stream hits the earth's magnetic field at 08:00 UT on June 7, 2015, and caused the IMF Bz (Figure 11b) to increase from ~0 nT to 13.85 nT for 8 hours (i.e., 12:00 UT to 20:00 UT). After which the IMF Bz oscillates from 23:00 UT on June 7 to 12:00 UT on June 8, 2015. The solar wind speed (Figure 11a) started to increase from 12:00 UT on June 7, 2015, and reached the maximum speed of 680km/s on June 8 at 12:00 UT. It remained above 600km/s until the early hours of June 11. From June 12 to June 13, the solar wind speed was below 600km/s; - and at early hours of June 14, till June 15, the solar wind speed was at 600km/s. On the late hours on June 16, we observed a surge in solar wind speed at 20:00 UT. This surge in solar wind speed caused a minor storm on June 17 as the solar wind speed was descending (Figure e).

During the increasing phase of the solar wind, the interplanetary electric field oscillates rapidly and reached the maximum eastward value of ~10mV/m at 06:00 UT and westward value of ~ -7mV/m from 08:00 until 12:00UT on June 8. The westward component of the auroral index (AL) reached the minimum value of -1000 nT at 08:00 UT on June 8. The SYM-H index increased from -14 nT to 30 nT for a period of 8 hours on June 7 when the solar wind stream hits the magnetosphere. It decreases rapidly from 00:00 UT and reached the minimum value of -105 nT at 07:45 UT on June 8, 2015. The recovery phase starts immediately. During the recovery phase, the EEJ amplitude presents a greater magnitude than the five days magnetically quiet average (Figure 11f). On June 8 and 9, we observed an increase in the magnitude of EEJ which are 60 nT at 16:00 UT and 61 nT at 18:00 UT respectively. And from June 10 until June 17, the amplitude of the Five magnetically quiet days average shows a greater magnitude than the disturbed days. On June 15, we observed a notable westward flow of EEJ during the daytime which is associated with the enhanced auroral sub-storm at high-latitude and the arrival of the westward disturbance equatorward wind at the low-latitude in Brazilian region. Also on June 17, during the recovery phase of the weak storm, we observed fluctuations in EEJ during the daytime which also correlates with the increase in the magnitude of the auroral sub-storm. The daytime westward flow of the EEJ signals the arrival of the westward disturbance dynamo electric field.

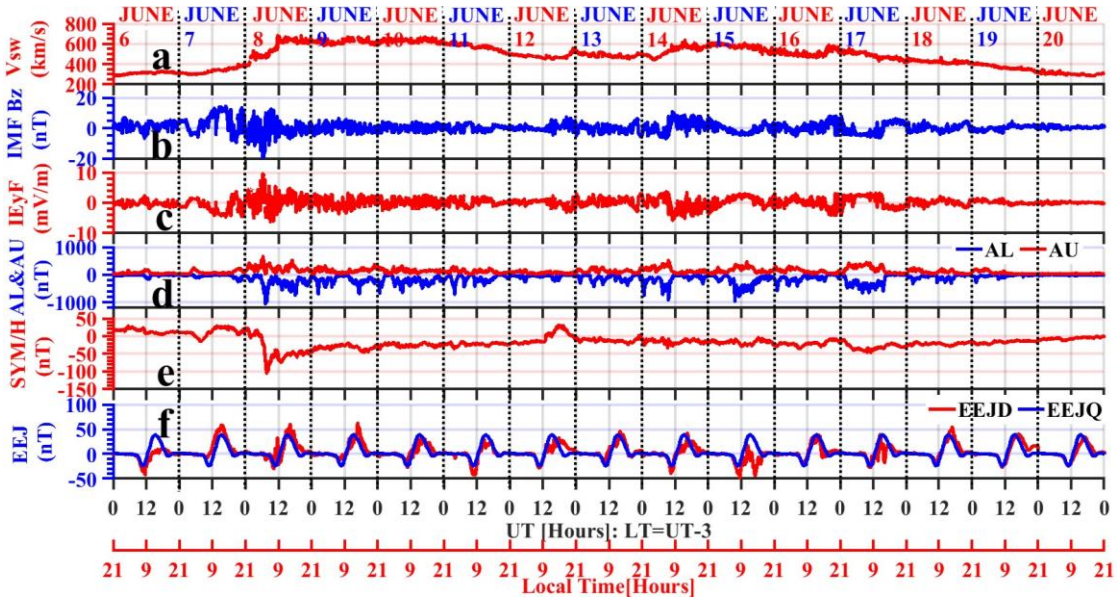

Figure 11. - Global parameters from June 6 -20, 2015. (a) displays the velocity of the solar wind. (b) exhibits the IMF Bz (Interplanetary magnetic field in the Z direction), (c) presents the interplanetary electric field, (d) portrays the aurora electrojet (AL: aurora lower boundary, AU: aurora upper boundary), (e) demonstrates the H-component symmetry of Earth's magnetic field observed at various low-latitudes, and lastly, (f) illustrates the equatorial electrojet (EEJ).

3.2.2. DP2 Fluctuations at Brazilian Longitude

Preprints (www.preprints.org) | NOT PEER-REVIEWED | Posted: 3 October 2023 doi:10.20944/preprints202310.0108.v1

Figure 12 presents the temporal variation of IMF Bz alongside with dBz and DP2 signals from June 6 to 20, 2015. From the Figure 12a, the southward turning of IMF Bz around 06:00 UT on June 8, was not geoeffective in the Brazilian longitude because it was on the nightside. But we observed rapid oscillations of the DP2 (in Figure 12c) during the daytime which corresponds with the increase in the EEJ during the daytime. Figure 12c shows the overlapping plot of the DP2 oscillations at Belem (Red) and Alta Floresta (Blue). It is clear that the oscillation of the DP2 current is significant at Belem than at the Alta Floresta due to the cowling conductivity effect at the Belem.

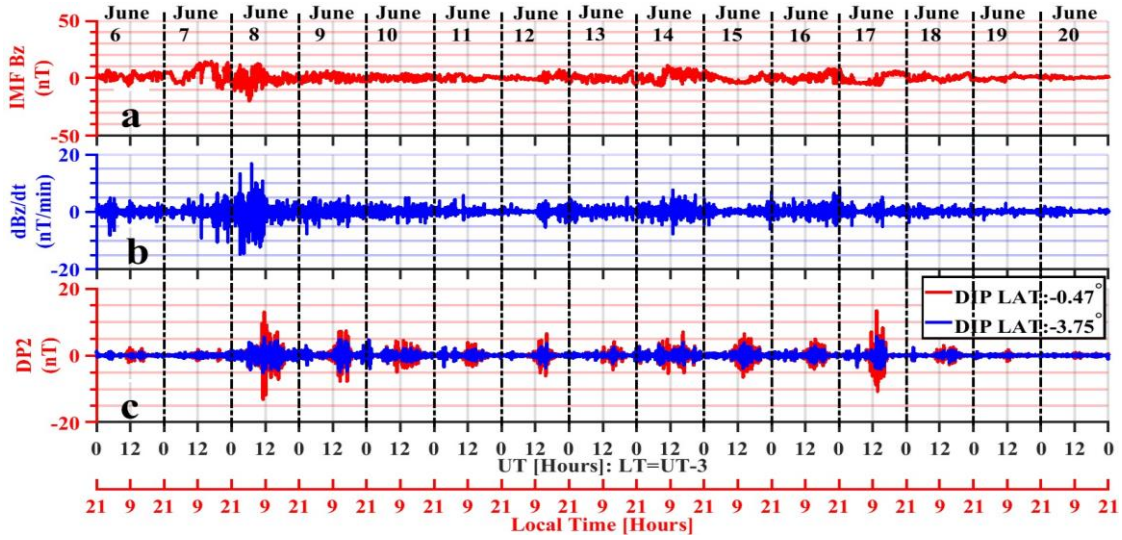

Figure 12. Variations of IMF Bz along with dBz and DP2. (a) displays IMF Bz, (b) shows dBz/dt, (c) illustrates DP2.

3.2.3. Diurnal Component of Disturbance Dynamo

Figure 13 depicts the variation of the Akasofu parameter that demonstrates the coupling of the solar wind and the magnetosphere (blue colour on the left-hand side), the AE index (red colour on the right-hand side: Figure 13a), ASYM-H index is shown in Figure 13b, and the diurnal component of the D_{dyn} at the magnetometer station in Belem (red colour), and in Alta Floresta (blue colour, Figure 13c). From Figure 13a, we observed that the solar wind stream transferred energy and momentum into the magnetosphere on June 8, 2015, from 0:00 UT to 08:00 UT. And another significant energy was transferred on June 14 when there was an increase in the solar wind speed stream. The H-component of the earth's magnetic field measured at the mid-latitude by chains of the magnetometer confirmed the energy input into the earth's magnetic field on June 8. On June 15, the maximum eastward strength of D_{dyn} in Belem is 12 nT at 04:00 UT (01:00 LT) and minimum westward strength is -20 nT at 16:00 UT (13:00 LT) while the maximum eastward strength of D_{dyn} in Alta Floresta is 7 nT at 07:00 UT (04:00 LT) and minimum westward strength is -12.28 nT at 17:30 UT (14:30 LT). On June 16, the maximum eastward strength of D_{dyn} is 17 nT at 03:30 UT (0:30 LT) and minimum westward is -14 nT at 17:30 UT (14:30 LT) in Belem and in Alta Floresta, the maximum eastward strength is 11 nT at 05:30 UT (02:30 LT) and minimum westward strength is -10.52 nT at -19:00 UT (16:00 LT). And lastly on June 17, the maximum eastward strength of D_{dyn} is 15.0 nT at 06:00 UT (03:00 LT) and minimum westward at -13.39 nT at 16:00 UT (13:00 LT) in Belem and in Alta Floresta, the maximum eastward strength of D_{dyn} is 12 nT at 06:00 UT (03: 00 LT) and the minimum westward strength is -10.85 nT at 17:00 UT (14:00 LT). We can see that D_{dyn} strength is larger at Belem than at Alta Floresta.

Preprints (www.preprints.org) | NOT PEER-REVIEWED | Posted: 3 October 2023 doi:10.20944/preprints202310.0108.v1

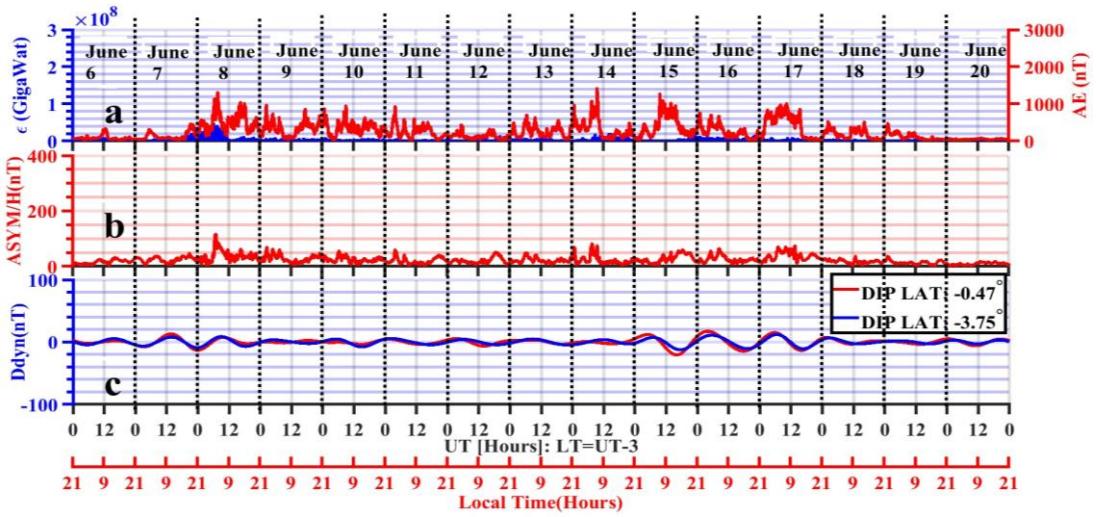

Figure 13. Variation of the Diurnal component of D_{dyn} alongside with Akasofu parameter, AE index and ASYM-H index. (a) The left-hand side displays the AE index, while the right-hand side shows the Akasofu index. (b) Depicts the AYSM-H index, which represents the response to auroral substorms at high latitudes, (c) presents the development of $\mathbf{D_{dyn}}$ at Belem (indicated by the red legend) and Alta Floresta (indicated by the blue legend).

3.2.4. Development of D_{dyn} during the June 8 Geomagnetic Storm.

Figure 14 has the same format as Figure 6. We observed the development of D_{dyn} from June 15 to June 17, 2015. On June 15, the period of D_{dyn} ranges from 12 hours to 32 hours periodicities

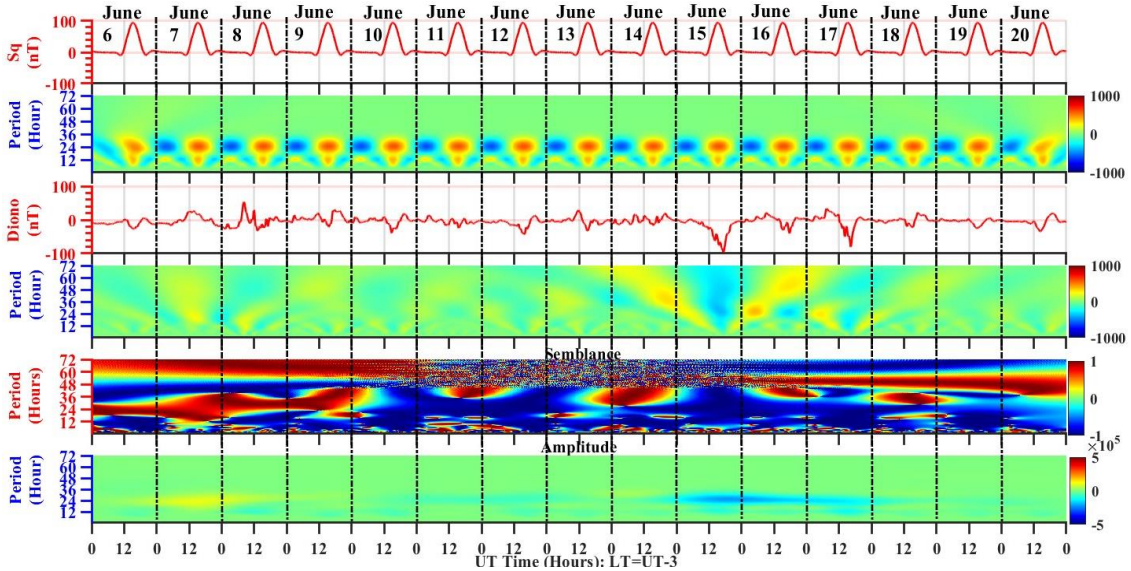

Figure 14. illustrates the relationship between Sq current and Diono current, showcasing both phase correlation and anti-correlation. (a)The average Sq current is displayed over a period of five geomagnetically quiet days in June 2015. (b) exhibits the continuous wavelet transform of the Sq current depicted in (a). (c) represents the Diono current observed from June 20 to 30, 2015. The continuous wavelet transform of the Diono current in Figure 6c is shown in (d). (e) presents a map indicating the anti-correlation (-1) and correlation semblance (+1) between Diono and Sq current. Lastly, (f) displays the amplitude of the semblance analysis.

3.2.5. Effect of Cowling Conductivity on D_{dyn} Strength

Figure 15 follows the same format as Figure 7, presenting a similar trend. In Figure 15b and c, we present the normalized $\boldsymbol{D_{dyn}}$ amplitude at both Belem and Alta Floresta. Notably, the strength of Ddyn at Belem was found to be higher compared to Alta Floresta. This discrepancy can be attributed to the varying cowling conductivity effect, which is stronger at Belem than at Alta Floresta.

Preprints (www.preprints.org) | NOT PEER-REVIEWED | Posted: 3 October 2023 doi:10.20944/preprints202310.0108.v1

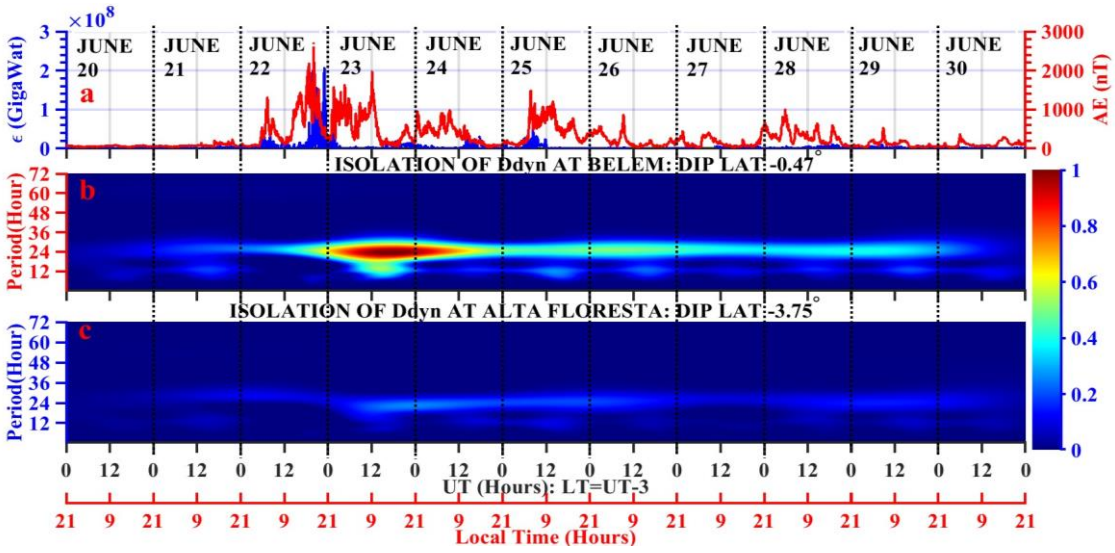

Figure 15. D_{dyn} Development at Belem and Alta Floresta. (a), the AE index is displayed on the right-hand side, while the Akasofu parameter is shown on the left-hand side. (b) presents the amplitude of Ddyn specifically at Belem. Lastly, (c) illustrates the amplitude of Ddyn at Alta Floresta.

3.2.6. Impact of Magnetic Perturbation on VTEC from June 8-20, 2015.

Figure 16 presents the temporal variation of VTEC from June 6-20, 2015. We observed a positive ionospheric storm on VTEC at all the stations during the early stage of the June 8 geomagnetic storm recovery day. The positive ionospheric storm corresponds with the increase in the magnitude of the vertical drift velocity (Figure 16b) that will be estimated from the ground-based magnetometer. On June 15, the five magnetically quiet days average VTEC is greater than the disturbed day value of VTEC. Therefore, we observed negative ionospheric storm at -12.51° dip latitude on June 15, June 17, and June 19.

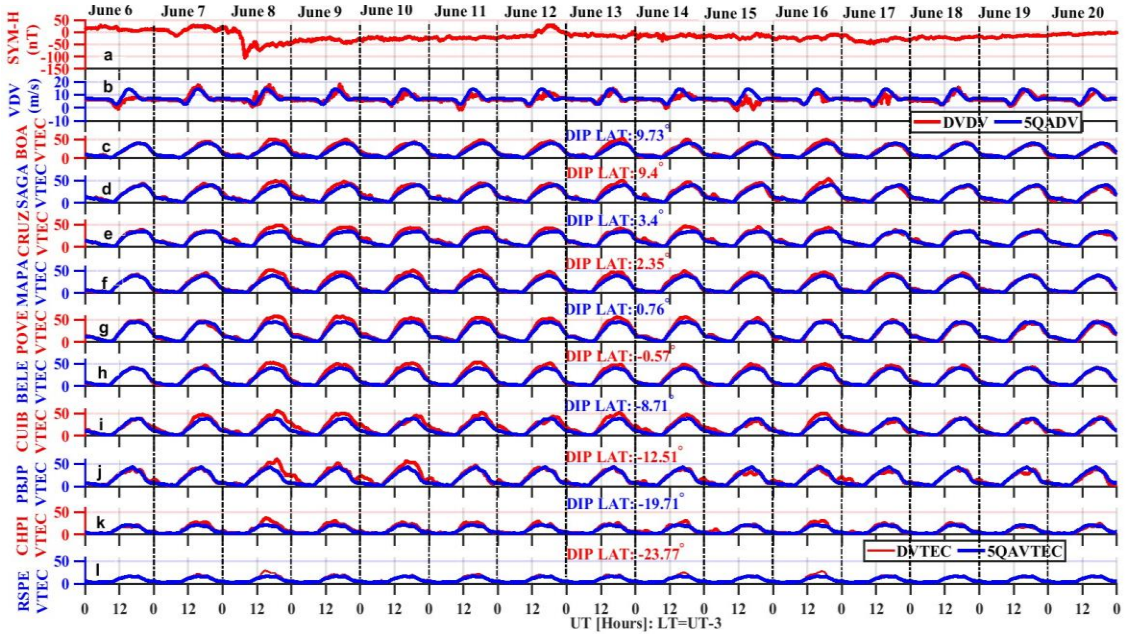

Figure 16. Temporal variation of VTEC from June 6 to June 20, 2015. (a) shows the day-to-day variation of the SYM-H index. (b) presents the vertical drift velocity that we estimated from ground-based magnetometer from June 20 to 30, 2015 (blue legend (five magnetically quiet days average), red legend (vertical drift velocity from June 20 to 30)). (c) to (l) present the temporal variation of VTEC at different latitudes from June 6 to 20, 2015.

3.2.7. Spatial – Temporal variation of VTEC from June 6-20, 2015

Preprints (www.preprints.org) | NOT PEER-REVIEWED | Posted: 3 October 2023 doi:10.20944/preprints202310.0108.v1

Figure 17 depicts the spatial and temporal variation of VTEC from June 6 to June 20, 2015. The geomagnetic storm main phase lasted for ~5 hours on June 8 (that is, from 04:00 UT to 08:00 UT). We observed a positive ionospheric storm during the early stage of the recovery phase which is more intense (ranging from 10 TECu to 20 TECu) between -2° and -12° dip latitude from 12:00 UT on June 8 until 01:00 UT on June 9, 2015. On June 15, from -8° to -12° dip latitude, starting from 14:00 UT to 20:00 UT, we observed the occurrence of a negative ionospheric storm which ranges between -10 TECu and -20 TECu. There is no GUVI satellite imagery for the period for the Brazilian longitude.

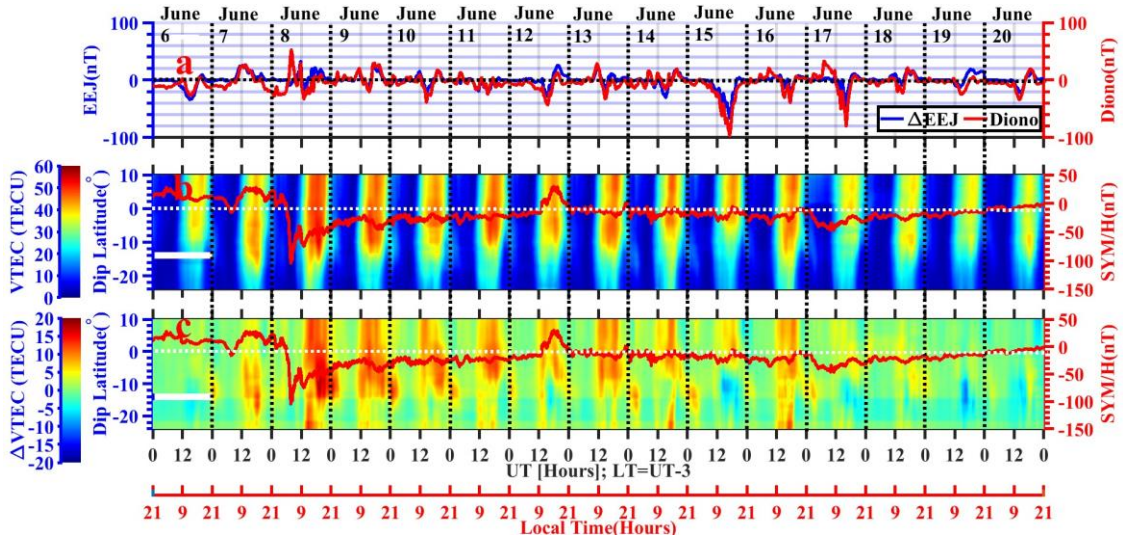

Figure 17. illustrates the spatial-temporal variation of *VTEC* alongside with Δ*EEJ* and $\boldsymbol{D_{iono}}$. (a) Change in *EEJ* and $\boldsymbol{D_{iono}}$ current from June 6 to June 20, 2015. (b) Day-to-day variation of *VTEC* (left-hand side) and *SYM-H* index (right-hand side). (c) Change in *VTEC* from June 6 to June 20, 2015, (left-hand side) and SYM-H index on right-hand side.

3.3. SAMI2 Model Run Results.

In this section, we will explore the performance of the SAMI2 Model during the westward disturbance dynamo event that occurred on June 23, 2015. To achieve this, we utilized two different vertical drift velocities as inputs into the SAMI2 code.

The SAMI2 Model is a flexible physics-based model designed for low-to-middle latitude regions. It simulates the dynamic and chemical changes in the ionosphere [47], [48], [61]. By default, the SAMI2 model assumes that the vertical ExB drift magnetic field in the ionosphere follows either a sinusoidal pattern or is specified by the ExB drift model.

Initially, we used the SAMI2 code's default ExB drift velocity model, and the corresponding outcome is depicted in Figure 18. Subsequently, we replaced the default ExB drift velocity with the EXB drift derived from the ground-based magnetometer data for the daytime period. The result of this substitution is presented in Figure 19.

In Figure 18, we observe that the default E × B drift in the SAMI2 model fails to replicate the impact of the westward disturbance dynamo on VTEC on June 23. The blue legend corresponds to magnetically disturbed days, while the red legend represents a magnetically quiet reference day (June 20, 2015). Interestingly, the default E × B drift estimates a higher value for the disturbed day influenced by the westward disturbance dynamo compared to the quiet reference day. This outcome significantly differs from the actual observations made on the GPS VTEC (Vertical Total Electron Content) on June 23, 2015.

However, in Figure 19, we replaced the default E × B drift with an E × B drift estimated from the ground-based magnetometer. As shown in Figure 19, this alteration in the SAMI2 model successfully reproduces the effect of the westward disturbance dynamo on the VTEC, which aligns more closely with the observations data.

Preprints (www.preprints.org) | NOT PEER-REVIEWED | Posted: 3 October 2023 doi:10.20944/preprints202310.0108.v1

In summary, the SAMI2 model's default E × B drift failed to capture the westward disturbance dynamo's influence on VTEC, but when we utilized the E × B drift estimated from the ground-based magnetometer data, the model successfully reproduced the observed impact on VTEC on June 23, 2015.

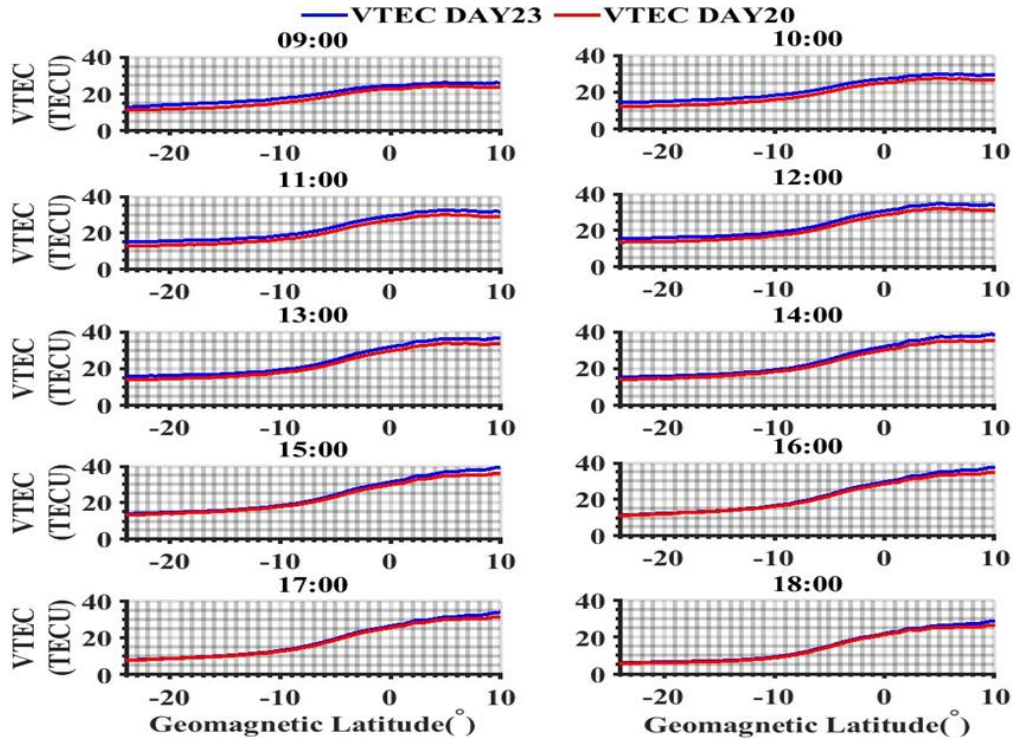

Figure 18. SAMI2 Modeling of the Brazilian equatorial and Low-latitude during westward disturbance Dynamo event on 23 June 2015 using Scherliess and Fejer EXB drift Model as an input into SAMI2 code.

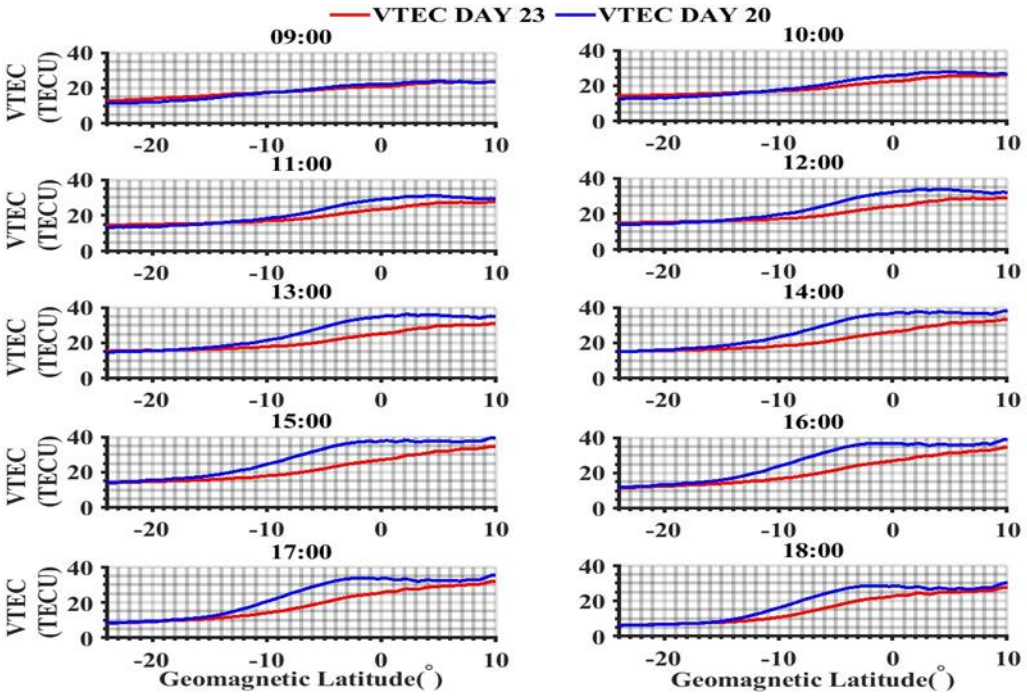

Figure 19. SAMI2 Modeling of the Brazilian equatorial and Low-latitude during westward disturbance Dynamo event on 23 June 2015 by using the EXB vertical drift estimated from the ground-based magnetometer as input into SAMI2 code.

4. Discussion

 doi:10.20944/preprints202310.0108.v1

In this section, our focus is on exploring the fluctuations of VTEC (Vertical Total Electron Content) and magnetic disturbances in the ionosphere over the Brazilian equatorial and low-latitude regions. Moreover, we investigated the impact of thermospheric composition change on the occurrence of both positive and negative ionospheric storms.

4.1. Effect of Geomagnetic Storm on Electric Field.

In June, we conducted a study to examine the changes in the ionospheric electric field during a geomagnetic storm, specifically focusing on the under-shielding field-aligned current of the R1 region. This geomagnetic storm, which occurred on June 22–23, 2015, ranked as the second most intense event during solar cycle 24 [24], [25].

During the storm's main phase on June 22, 2015, from 19:00 UT to 20:00 UT, we observed a significant increase of approximately 88 nT in the Equatorial Electrojet (EEJ) compared to its peak value of 12.52 nT recorded on June 21 (Figure 3f). We attribute the enhancement in the EEJ to the eastward prompt penetration of the Magnetospheric convection electric field due to the under-shielding of the R1 region field-aligned current [13], [33], [47–49].

Notably, on June 22, the peak of the eastward interplanetary field reached 27 mV/m on the dayside during the main phase, further contributing to the observed changes in the ionospheric electric field.

Subsequently, on June 23, 2015, we observed a westward flow of the EEJ starting from 10:00 LT and lasting until around 20:00 LT in the Brazilian longitude. This westward flow indicated further dynamic changes in the ionospheric electric field during the aftermath of the geomagnetic storm.

Top of Form

On June 23, between 12:00 UT and 15:00 UT, the maximum amplitude of the westward Electrojet (EEJ) was recorded to be -146.76 nT. This westward EEJ is attributed to the presence of a westward disturbance dynamo electric field.

The origin of the equatorward-directed disturbance thermospheric wind is a result of magnetospheric energy input at high latitudes. This energy input leads to the joule heating and collisional interaction of neutrals with rapidly convecting ions under a strong electric field in high latitudes. Initially, the disturbance winds from auroral heating move equatorward, but due to the Coriolis effect, they acquire a westward velocity relative to the Earth.

The equatorward Pedersen current, formed by the westward disturbance wind over mid-latitudes, tends to positively charge the ionosphere at low latitudes until it is interrupted by the subsequent poleward electric field. In the southern (northern) hemisphere mid-latitudes, this poleward electric field, perpendicular to the upward (downward) directed magnetic field lines, induces a westward plasma drift and an eastward hall current. At the terminators, where the hall current is cut off, two current loops are created, generating a dusk-to-dawn electric field.

This dusk-to-dawn electric field, extending through the conducting ionosphere, influences low and equatorial latitudes. It should be noted that this low latitude current vortex differs in orientation and polarity from the typical Sq current vortex and the magnetic quiet time wind dynamo electric field. References: [5], [16], [17], [19], [23], [32–35], [47].

The geomagnetic storm that occurred on June 8, 2015 (Figure 11), was solely driven by a High-speed solar wind stream (HSSWs), with the maximum solar wind speed reaching 680.4 km/s around 09:30 LT during the recovery phase (see Figure 11a). At approximately 3:30 LT, the Interplanetary Magnetic Field (IMF) Bz turned southward, with the maximum southward incursion measuring -20 nT (Figure 11b). Concurrently, the interplanetary electric field turned eastward and peaked at 10 mV/m (Figure 11c).

During the storm, the westward auroral substorm reached its maximum amplitude at around 04:00 LT, measuring -1000 nT (see Figure 11d), while the southward amplitude of the SYMH-index was -105 nT. Interestingly, the response of the Equatorial Electrojet (EEJ) to the eastward penetration of the magnetospheric electric field was delayed by approximately four hours (Figure 11f).

Comparing the values of the EEJ, we observed that on June 6, the early morning counter electrojet was absent on June 8, 2015. The EEJ value at 08:00 LT on June 8, 2015, was 32.24 nT. Moreover, we

Preprints (www.preprints.org) | NOT PEER-REVIEWED | Posted: 3 October 2023 doi:10.20944/preprints202310.0108.v1

noticed an enhancement in EEJ on the day after the main phase, on June 9, 2015. On June 25, there was a decrease in the amplitude of EEJ in Figure 11f.

However, when comparing the value of the EEJ during the main phase of the geomagnetic storm on June 22-23, 2015, we found it to be greater than the value observed during the main phase on June 8, 2015. We attributed this large difference to the amplitude of the Eastward prompt penetration of the magnetospheric convection electric field (EPPMEF). Specifically, on June 22, the IEyF (y-component Interplanetary Electric Field) was 27 mV/m, while it was 10 mV/m on June 8, 2015. Consequently, the EPPMEF on June 22 was approximately three times greater than the EPPMEF observed during the June 8, 2015 storm.

4.2. Development of Positive and Negative ionospheric

Enhancement (suppression) of the equatorial electric field during the occurrence of a geomagnetic storm plays a crucial role in the formation of the positive (negative) ionospheric storm. Figures 8 and 9 present the day-to-day variation of VTEC at different dip latitudes and the spatial and temporal variation of VTEC respectively between June 20 and June 30. On June 22, 2015, the positive ionospheric storm in the southern hemisphere spanned from -6° to -24° dip latitude. During this period, an eastward prompt penetration magnetospheric electric field (EPPMEF) superimpose on the quiet time eastward electric field and strengthened the vertical drift velocity, so that the ionosphere was lifted to high altitudes of low recombination rate. So therefore, the plasma was removed from the equator and deposited at a higher latitude (altitude) where recombination is very slow. The mechanical effect of the storm time equatorward wind also contributed to the formation of the positive ionospheric storm by increasing the $[\boldsymbol{O}]/[\boldsymbol{N_2}]$ $\boldsymbol{ratio}$. And also, when we examined the GUVI satellite image in Figure 10, we observed an increase in the thermospheric $[\boldsymbol{O}]/[\boldsymbol{N_2}]$ ratio on June 22. We observed another positive ionospheric storm on June 25 which also correlates with the enhancement in Vertical drift velocity. On June 22, the thermospheric $[\boldsymbol{O}]/[\boldsymbol{N_2}]$ ratio was ~ 0.7 and on June 25 thermospheric $[\boldsymbol{O}]/[\boldsymbol{N_2}]$ was ~0.6. On June 23, a major negative ionospheric storm occurs. It started from ~10° to ~ -20° dip latitude. The occurrence of the negative ionospheric storm on June 23, June 24, June 26, June 27, June 28, and June 29 was due to the effect of the westward disturbance dynamo electric field at the equatorial and low latitude Brazilian ionosphere during the daytime. The intensity of the negative storms corresponds with the westward EEJ during the daytime.

During the main phase of the June 8, 2015, geomagnetic storm, there was no enhancement in the VTEC. But we observed a positive ionospheric storm during the early stage of the recovery phase (Figure 16 and 17). On June 8, 2015, we observed a positive ionospheric storm from the northern hemisphere to the southern hemisphere. Unlike the 22-23 June geomagnetic storm, in which the positive ionospheric storm was intense in the southern hemisphere only. the positive ionospheric storms were localized around the magnetic dip latitude. This can be attributed to the weak enhancement in the equatorial electric field during the main phase of the June 8 geomagnetic storm. The negative ionospheric storm on the June 15, was due to an enhancement in the westward electric field during daytime.

4.3. Eastward and Westward Disturbance Dynamo

Figures 5 and 7 present the development of the Ddyn during the geomagnetic storm of June 22-23, and 25, 2015. The $\boldsymbol{D_{dyn}}$ amplitude has a period of 12 to 32 hours on June 23 but the amplitude was confined to 24 hours from June 24 to June29, 2015 (Figure 7). Figures 13 and 15 present the development of Ddyn during the storm of June 8, 2015. The Ddyn strong amplitude began to form on June 15 and persisted until June 17 (Figure 15). The positive ionospheric storm in Brazilian longitude during the night is related to the eastward component of the Ddyn during the night, whereas the negative ionospheric storm is related to the westward dynamo electric field.

4.4. SAMI2 Model performance during the D_{dyn} event.

The performance of the SAMI2 model was assessed during the disturbance dynamo electric field event on June 23, 2015. We conducted simulations using the SAMI2 model for the Brazilian

 doi:10.20944/preprints202310.0108.v1

equatorial and low-latitude ionosphere, considering two different ExB drift velocities. In the first case, we utilized the default ExB drift velocity, as illustrated in Figure 18. However, the default ExB drift velocity failed to replicate the impact of the westward disturbance dynamo electric field on the simulated VTEC (Vertical Total Electron Content).

To address this limitation, we replaced the default ExB drift velocity with the vertical drift velocity estimated from the ground-based magnetometer. With this adjustment, the SAMI2 model successfully reproduced the effect of the westward disturbance dynamo electric field on simulated VTEC, as depicted in Figure 19.

Notably, the SAMI2 model's findings indicated that the depletion of VTEC was particularly pronounced near the station situated close to the dip equator. This observation implies that the equatorial ionosphere experienced a significant reduction in altitude, resulting in a higher recombination rate.

In conclusion, the SAMI2 model's performance was enhanced when incorporating the estimated vertical drift velocity, which allowed for a more accurate representation of the westward disturbance dynamo electric field's influence on VTEC. This, in turn, shed light on the intense VTEC depletion around the dip equatorial stations, highlighting the equatorial ionosphere's descent to low altitudes with a notable increase in recombination rate.

5. Conclusion

The following is the summary of our discoveries regarding the response of the Brazilian equatorial and low-latitude ionosphere during the occurrences of the geomagnetic storms of June 8, 22-23, and, 25, 2015: -

i. The positive ionospheric storm's development results from a combination of factors, including an increased [O]/[N_2] ratio in the thermosphere, the eastward penetration of the magnetospheric electric field, and the equatorward wind that carries a higher concentration of oxygen atoms compared to nitrogen molecules. The observed nighttime positive ionospheric storm in the Brazilian longitude shows a correlation with the eastward disturbance dynamo [47].

ii. On 23 June 2015, as depicted in Figures 5, 7, 9, and 10, the occurrence of the negative ionospheric storm can be attributed to two key factors: a reduction in the thermospheric [O]/[N_2] ratio and the presence of a westward disturbance dynamo electric field. These elements were observed to be directly linked to the development of the negative ionospheric storm [13], [55], [56], [62], [63].

iii. The amplitude of Ddyn's development during a geomagnetic storm, which arose from the combined effects of a coronal mass ejection (CME) (see Figure 7) and high-speed solar wind streams (HSSWs), is significantly larger and lasts for several days when compared to the geomagnetic storm (see Figure 15) driven solely by HSSWs. Moreover, the cowling conductivity plays a crucial role in amplifying the Ddyn amplitude, as observed in the Belem (dip lat: -0.47°) and Alta Floresta (dip alt: -3.75°) regions.

iv. Furthermore, a strong agreement was noted in the results obtained from the two methods used to isolate DP2 and Ddyn from Diono.

v. In order to optimize the SAMI2 model's performance during a period of intense westward development of the disturbance dynamo in the daytime, it is essential to integrate the storm time equatorward wind into the SAMI2 model [19].

References

1. D. Knipp, Understanding Space Weather and the Physics Behind It. 2011.
2. M. A. Abdu, "Outstanding problems in the equatorial ionosphere-thermosphere electrodynamics relevant to spread F," 2001. [Online]. Available: www.elsevier.nl/locate/jastp
3. M. E. Greenspan, C. E. Rasmussen, W. J. Burke, and M. A. Abdu, "Equatorial density depletions observed at 840 km during the great magnetic storm of March 1989," *J Geophys Res Space Phys*, vol. 96, no. A8, pp. 13931–13942, Aug. 1991, doi: 10.1029/91ja01264.
4. N. Balan, I. S. Batista, M. A. Abdu, J. MacDougall, and G. J. Bailey, "Physical mechanism and statistics of occurrence of an additional layer in the equatorial ionosphere," *J Geophys Res Space Phys*, vol. 103, no. A12, pp. 29169–29181, Dec. 1998, doi: 10.1029/98ja02823.

5. E. R. de Paula *et al.*, "Ionospheric irregularity behavior during the September 6–10, 2017 magnetic storm over Brazilian equatorial–low latitudes," *Earth, Planets and Space*, vol. 71, no. 1, p. 42, Dec. 2019, doi: 10.1186/s40623-019-1020-z.
6. R. Raghavarao, L. E. Wharton, N. W. Spencer, H. G. Mayr, and L. H. Brace, "An equatorial temperature and wind anomaly (ETWA)," *Geophys Res Lett*, vol. 18, no. 7, pp. 1193–1196, Jul. 1991, doi: 10.1029/91GL01561.
7. N. Mridula and T. K. Pant, "On the possible role of zonal dynamics in the formation and evolution of F3 layers over equator," *J Atmos Sol Terr Phys*, vol. 134, pp. 69–77, Nov. 2015, doi: 10.1016/j.jastp.2015.09.019.
8. N. Mridula, T. K. Pant, and G. Manju, "On the variability of the Equatorial Ionization Anomaly Trough over Indian region: A novel analysis using Beacon TEC measurements," *Advances in Space Research*, vol. 66, no. 3, pp. 646–654, Aug. 2020, doi: 10.1016/j.asr.2020.04.040.
9. E. v. APPLETON, "Two Anomalies in the Ionosphere," *Nature*, vol. 157, no. 3995, pp. 691–691, May 1946, doi: 10.1038/157691a0.
10. L. Jose, S. Ravindran, C. Vineeth, T. K. Pant, and S. Alex, "Investigation of the response time of the equatorial ionosphere in context of the equatorial electrojet and equatorial ionization anomaly," *Ann Geophys*, vol. 29, no. 7, pp. 1267–1275, 2011, doi: 10.5194/angeo-29-1267-2011.
11. N. Balan, J. Souza, and G. J. Bailey, "Recent developments in the understanding of equatorial ionization anomaly: A review," *J Atmos Sol Terr Phys*, vol. 171, pp. 3–11, Jun. 2018, doi: 10.1016/j.jastp.2017.06.020.
12. J. H. Sastri, "Equatorial anomaly in F-region-A review," 1990.
13. N. Balan, L. Liu, and H. Le, "A brief review of equatorial ionization anomaly and ionospheric irregularities," *Earth and Planetary Physics*, vol. 2, no. 4, pp. 1–19, 2018, doi: 10.26464/epp2018025.
14. N. Balan, H. Alleyne, Y. Otsuka, D. Vijaya Lekshmi, B. G. Fejer, and I. McCrea, "Relative effects of electric field and neutral wind on positive ionospheric storms," *Earth, Planets and Space*, vol. 61, no. 4, pp. 439–445, Apr. 2009, doi: 10.1186/BF03353160.
15. M. Piersanti *et al.*, "Comprehensive Analysis of the Geoeffective Solar Event of 21 June 2015: Effects on the Magnetosphere, Plasmasphere, and Ionosphere Systems," *Sol Phys*, vol. 292, no. 11, p. 169, Nov. 2017, doi: 10.1007/s11207-017-1186-0.
16. M. A. Abdu, J. H. Sastri, J. MacDougall, I. S. Batista, and J. H. A. Sobral, "Equatorial disturbance dynamo electric field longitudinal structure and spread F: A case study from GUARA/EITS campaigns," *Geophys Res Lett*, vol. 24, no. 13, pp. 1707–1710, 1997, doi: 10.1029/97GL01465.
17. M. A. Abdu, J. R. de Souza, J. H. A. Sobral, and I. S. Batista, "Magnetic storm associated disturbance dynamo effects in the low and equatorial latitude ionosphere," 2006, pp. 283–304. doi: 10.1029/167GM22.
18. J. Rodríguez-Zuluaga, S. M. Radicella, B. Nava, C. Amory-Mazaudier, H. Mora-Páez, and K. Alazo-Cuartas, "Distinct responses of the low-latitude ionosphere to CME and HSSWS: The role of the IMF Bz oscillation frequency," *J Geophys Res Space Phys*, vol. 121, no. 11, pp. 11,528-11,548, Nov. 2016, doi: 10.1002/2016JA022539.
19. C. Amory-Mazaudier, O. S. Bolaji, and V. Doumbia, "On the historical origins of the CEJ, DP2, and Ddyn current systems and their roles in the predictions of ionospheric responses to geomagnetic storms at equatorial latitudes," *J Geophys Res Space Phys*, vol. 122, no. 7, pp. 7827–7833, Jul. 2017, doi: 10.1002/2017JA024132.
20. B. Nava *et al.*, "Middle- and low-latitude ionosphere response to 2015 St. Patrick's Day geomagnetic storm," *J Geophys Res Space Phys*, vol. 121, no. 4, pp. 3421–3438, Apr. 2016, doi: 10.1002/2015JA022299.
21. P. O. Amaechi *et al.*, "Ground-Based GNSS and C/NOFS Observations of Ionospheric Irregularities Over Africa: A Case Study of the 2013 St. Patrick's Day Geomagnetic Storm," *Space Weather*, vol. 19, no. 2, Feb. 2021, doi: 10.1029/2020SW002631.
22. M. Blanc, S. Profile, and A. D. Richmond, "THE IONOSPHERIC DISTURBANCE DYNAMO," 1980. [Online]. Available: https://www.researchgate.net/publication/349725008
23. W. Younas, C. Amory-Mazaudier, M. Khan, and R. Fleury, "Ionospheric and Magnetic Signatures of a Space Weather Event on 25–29 August 2018: CME and HSSWs," *J Geophys Res Space Phys*, vol. 125, no. 8, Aug. 2020, doi: 10.1029/2020JA027981.
24. C. Amory-Mazaudier, "Magnetic Signatures of Large-Scale Electric Currents in the Earth's Environment at Middle and Low Latitudes," *Atmosphere (Basel)*, vol. 13, no. 10, p. 1699, Oct. 2022, doi: 10.3390/atmos13101699.

25. V. H. Vasyliunas, "Mathematical model of magnetospheric convection and its coupling to the ionosphere. In Particles and Fields in the Magnetosphere," *Mc Cormac, B.M., Ed.; D. Reidel Publ. Co.: Dordrecht, The Netherlands*, 1970.
26. G. A. Mansilla, "Ionospheric Response to the Magnetic Storm of 22 June 2015," *Pure Appl Geophys*, vol. 175, no. 3, pp. 1139–1153, Mar. 2018, doi: 10.1007/s00024-017-1741-5.
27. E. Astafyeva, I. Zakharenkova, J. D. Huba, E. Doornbos, and J. IJssel, "Global Ionospheric and Thermospheric Effects of the June 2015 Geomagnetic Disturbances: Multi-Instrumental Observations and Modeling," *J Geophys Res Space Phys*, vol. 122, no. 11, Nov. 2017, doi: 10.1002/2017JA024174.
28. E. Astafyeva *et al.*, "Study of the Equatorial and Low-Latitude Electrodynamic and Ionospheric Disturbances During the 22–23 June 2015 Geomagnetic Storm Using Ground-Based and Spaceborne Techniques," *J Geophys Res Space Phys*, vol. 123, no. 3, pp. 2424–2440, Mar. 2018, doi: 10.1002/2017JA024981.
29. B. Paul, B. K. De, and A. Guha, "Latitudinal variation of F-region ionospheric response during three strongest geomagnetic storms of 2015," *Acta Geodaetica et Geophysica*, vol. 53, no. 4, pp. 579–606, Dec. 2018, doi: 10.1007/s40328-018-0221-4.
30. P. O. Amaechi, E. O. Oyeyemi, and A. O. Akala, "Geomagnetic storm effects on the occurrences of ionospheric irregularities over the African equatorial/low-latitude region," *Advances in Space Research*, vol. 61, no. 8, pp. 2074–2090, Apr. 2018, doi: 10.1016/j.asr.2018.01.035.
31. Gopi, "GPS-TEC analysis software," 2011. [Online]. Available: https://www.researchgate.net/publication/255978205
32. R. G. Rastogi, T. Kitamura, and K. Kitamura, "Geomagnetic field variations at the equatorial electrojet station in Sri Lanka, Peredinia," *Ann Geophys*, vol. 22, no. 8, pp. 2729–2739, Sep. 2004, doi: 10.5194/angeo-22-2729-2004.
33. C. Agodi Onwumechili, *THE EQUATORIAL ELECTROJET*. Overseas Publishers Association, 1997.
34. A. B. Rabiu, O. O. Folarin, T. Uozumi, N. S. Abdul Hamid, and A. Yoshikawa, "Longitudinal variation of equatorial electrojet and the occurrence of its counter electrojet," *Ann Geophys*, vol. 35, no. 3, pp. 535–545, Apr. 2017, doi: 10.5194/angeo-35-535-2017.
35. W. Younas, C. Amory-Mazaudier, M. Khan, and M. Le Huy, "Magnetic Signatures of Ionospheric Disturbance Dynamo for CME and HSSWs Generated Storms," *Space Weather*, vol. 19, no. 9, Sep. 2021, doi: 10.1029/2021SW002825.
36. N. M. Mene *et al.*, "Statistical study of the DP2 enhancement at the dayside dip-equator compared to low latitudes," *Ann Geophys*, vol. 29, no. 12, pp. 2225–2233, Dec. 2011, doi: 10.5194/angeo-29-2225-2011.
37. B. Nava *et al.*, "Middle- and low-latitude ionosphere response to 2015 St. Patrick's Day geomagnetic storm," *Journal of Geophysical Research A: Space Physics*, vol. 121, no. 4, pp. 3421–3438, Apr. 2016, doi: 10.1002/2015JA022299.
38. A. Nishida, " Coherence of geomagnetic DP 2 fluctuations with interplanetary magnetic variations ," *J Geophys Res*, vol. 73, no. 17, pp. 5549–5559, Sep. 1968, doi: 10.1029/ja073i017p05549.
39. A. Nishida, "Geomagnetic DP2 fluctuations and associated magnetospheric phenomena," *J Geophys Res*, vol. 73, no. 5, pp. 1795–1803, Mar. 1968, doi: 10.1029/JA073i005p01795.
40. N. E. Huang *et al.*, "The empirical mode decomposition and the Hilbert spectrum for nonlinear and non-stationary time series analysis," *Proceedings of the Royal Society of London. Series A: Mathematical, Physical and Engineering Sciences*, vol. 454, no. 1971, pp. 903–995, Mar. 1998, doi: 10.1098/rspa.1998.0193.
41. P. Flandrin, G. Rilling, and P. Goncalves, "Empirical Mode Decomposition as a Filter Bank," *IEEE Signal Process Lett*, vol. 11, no. 2, pp. 112–114, Feb. 2004, doi: 10.1109/LSP.2003.821662.
42. K. Dragomiretskiy and D. Zosso, "Variational Mode Decomposition," *IEEE Transactions on Signal Processing*, vol. 62, no. 3, pp. 531–544, Feb. 2014, doi: 10.1109/TSP.2013.2288675.
43. G. R. J. Cooper and D. R. Cowan, "Comparing time series using wavelet-based semblance analysis," *Comput Geosci*, vol. 34, no. 2, pp. 95–102, Feb. 2008, doi: 10.1016/j.cageo.2007.03.009.
44. "torrence and campo".
45. S. W. H. Cowley, "The Earth's magnetosphere: A brief beginner's guide," *Eos, Transactions American Geophysical Union*, vol. 76, no. 51, pp. 525–525, 1995, doi: 10.1029/95EO00322.
46. S.-I. Akasofu, "Energy coupling between the solar wind and the magnetosphere," *Space Sci Rev*, vol. 28, no. 2, 1981, doi: 10.1007/BF00218810.
47. J. D. Huba, G. Joyce, and J. A. Fedder, "Sami2 is Another Model of the Ionosphere (SAMI2): A new low-latitude ionosphere model," *J Geophys Res Space Phys*, vol. 105, no. A10, pp. 23035–23053, Oct. 2000, doi: 10.1029/2000ja000035.

48. J. D. Huba, G. Joyce, and J. A. Fedder, "The formation of an electron hole in the topside equatorial ionosphere," *Geophys Res Lett*, vol. 27, no. 2, pp. 181–184, Jan. 2000, doi: 10.1029/1999GL010735.
49. J. A. F. D. G. T. Richards P.G., "EUVAC: A solar EUV flux model for aeronomic calculations," *J. Geophys.Res., 99, 8981*, 1994.
50. B. G. Fejer and L. Scherliess, "Empirical models of storm time equatorial zonal electric fields," *J Geophys Res Space Phys*, vol. 102, no. A11, pp. 24047–24056, 1997, doi: 10.1029/97JA02164.
51. S. W. H. Cowley, "Magnetosphere-ionosphere interactions: A tutorial review," in *Geophysical Monograph Series*, vol. 118, Blackwell Publishing Ltd, 2000, pp. 91–106. doi: 10.1029/GM118p0091.
52. T. J. Fuller-Rowell, M. V. Codrescu, H. Rishbeth, R. J. Moffett, and S. Quegan, "On the seasonal response of the thermosphere and ionosphere to geomagnetic storms," *J Geophys Res Space Phys*, vol. 101, no. A2, pp. 2343–2353, Feb. 1996, doi: 10.1029/95ja01614.
53. A. D. F. M. W.G. BAKER, "ELECTRIC CURRENTS IN THE IONOSPHERE I. THE CONDUCTIVITY." [Online]. Available: https://royalsocietypublishing.org/
54. C. M. Huang, "Disturbance dynamo electric fields in response to geomagnetic storms occurring at different universal times," *J Geophys Res Space Phys*, vol. 118, no. 1, pp. 496–501, Jan. 2013, doi: 10.1029/2012JA018118.
55. T. J. Fuller-Rowell, M. V. Codrescu, H. Rishbeth, R. J. Moffett, and S. Quegan, "On the seasonal response of the thermosphere and ionosphere to geomagnetic storms," *J Geophys Res Space Phys*, vol. 101, no. A2, pp. 2343–2353, Feb. 1996, doi: 10.1029/95ja01614.
56. T. J. Fuller-Rowell, M. V. Codrescu, R. J. Moffett, and S. Quegan, "Response of the thermosphere and ionosphere to geomagnetic storms," *J Geophys Res*, vol. 99, no. A3, p. 3893, 1994, doi: 10.1029/93JA02015.
57. T. J. Fuller-Rowell, M. V. Codrescu, R. G. Roble, and A. D. Richmond, "How does the thermosphere and ionosphere react to a geomagnetic storm?," 1997, pp. 203–225. doi: 10.1029/GM098p0203.
58. T. Fuller-Rowell *et al.*, "Observed and modeled thermosphere and ionosphere response to superstorms," *Radio Sci*, vol. 42, no. 4, p. n/a-n/a, Aug. 2007, doi: 10.1029/2005RS003392.
59. Y. Wei, B. Zhao, G. Li, and W. Wan, "Electric field penetration into Earth's ionosphere: a brief review for 2000–2013," *Sci Bull (Beijing)*, vol. 60, no. 8, pp. 748–761, Apr. 2015, doi: 10.1007/s11434-015-0749-4.
60. N. Balan, L. Liu, and H. Le, "A brief review of equatorial ionization anomaly and ionospheric irregularities," *Earth and Planetary Physics*, vol. 2, no. 4, pp. 1–19, 2018, doi: 10.26464/epp2018025.
61. J. Klenzing, A. G. Burrell, R. A. Heelis, J. D. Huba, R. Pfaff, and F. Sim\~oes, "Exploring the role of ionospheric drivers during the extreme solar minimum of 2008," *Ann Geophys*, vol. 31, no. 12, pp. 2147–2156, 2013, doi: 10.5194/angeo-31-2147-2013.
62. N. Balan, J. Souza, and G. J. Bailey, "Recent developments in the understanding of equatorial ionization anomaly: A review," *J Atmos Sol Terr Phys*, vol. 171, pp. 3–11, Jun. 2018, doi: 10.1016/j.jastp.2017.06.020.
63. K. Liou, P. T. Newell, B. J. Anderson, L. Zanetti, and C. I. Meng, "Neutral composition effects on ionospheric storms at middle and low latitudes," *J Geophys Res Space Phys*, vol. 110, no. A5, 2005, doi: 10.1029/2004JA010840.